Applied Materials Today 40 (2024) 102366

Contents lists available at ScienceDirect

Applied Materials Today

journal homepage: www.elsevier.com/locate/apmt

Gradient ceramic structures via multi-material direct ink writing

Joshua Pelz [a,b], Nicholas Ku [b], Taylor Shoulders [b], Matthew Guziewski [b], Samuel Figueroa [a], Jeffrey J. Swab [b], Lionel R. Vargas-Gonzalez [b], Marc A. Meyers [a,*]

[a] University of California, San Diego, La Jolla, CA, 92093, United States
[b] DEVCOM Army Research Laboratory, Aberdeen Proving Ground, Aberdeen, MD, 21005, United States

ARTICLE INFO

Keywords:
Dynamic mechanical analysis
Failure/fracture mechanisms
Functionally graded material (FGM), Layered structures
Structure-property relationship
(Not in keyword index: additive manufacturing
Direct ink writing
Robocasting, etc.)

ABSTRACT

Dense boron carbide-silicon carbide specimens with composition tailored at the mesoscale were produced by direct ink write additive manufacturing in three configurations: I, 2 % and II, 10 % compositional layer-to-layer steps, and III, homogeneous composition throughout. Flexural strength, indicative of tensile failure, is the highest for the Type-II design (366 MPa) due to its compressive residual stress state in the surface layers. Analysis of thermally-induced residual stresses predicts the ranking of the flexural strengths obtained for Type-II (highest), Type-I (intermediate), and Type-III (lowest) specimens. Compressive strength is load-orientation independent, highly strain-rate dependent, and reduced for specimens with thermal residual stress. Mechanical tests were performed in cube and dumbbell geometries. Dumbbell geometry compression specimens have a compressive strength that is 68 % (quasistatic) and 86 % (dynamic) higher than that of cube geometry and show a greater strain rate dependence. The rate dependency is attributed to the competition between crack propagation and loading velocities. Type-I dumbbells show the highest mean compressive strength of 3.96 GPa (quasi-static) and 5.11 GPa (dynamic). The failure mode evolves from mixed intergranular/transgranular at low strain rates to transgranular at high strain rates. High-speed video analysis indicates that dumbbell geometry specimens fail in compression due to microcrack growth and coalescence, while cubes fail due to the axial macrocracks that develop at the specimen/load platen interface and propagate into the specimen parallel to the loading direction (end splitting). This work demonstrates the impact of compositional variation, tailored by additive manufacturing, on the mechanical performance of ceramic composites.

1. Introduction

Ceramic materials have flaw-sensitive mechanical properties, complicating production by additive manufacturing (AM) where processing flaws and incomplete densification are common. Extensive research on advanced ceramics aluminum oxide (Al_2O_3), silicon carbide (SiC), and boron carbide (B_4C), reveals that trends in mechanical properties follow density and microstructure [1]. Some examples can be found in the literature that demonstrate that monolithic ceramics produced via AM have the potential to achieve similar mechanical properties as those produced by conventional powder processing routes [2–4]. A combination of spark-plasma sintering and cold-isostatic pressing was used to reach 95 % relative density for AM boron carbide components, and resulted in a hardness of 27 GPa and a compressive strength of ~1800 MPa [3]. Alumina components fabricated by CODE, a direct ink writing technique, achieved a relative density of 98 % and 2.1 μm average grain size, resulting in mechanical properties equivalent to traditionally processed alumina, with a Young's modulus, fracture toughness, and hardness of 371 GPa, 4.5 MPa*$m^{0.5}$, and 19.8 GPa, respectively [4]. Still, the flaw-sensitivity of these materials remains a major challenge for technical application in dynamic environments. Al_2O_3, SiC, and B_4C are utilized in dynamic applications where they are subjected to strain rates up to 10^6 s^{-1} [5] and inertial effects dominate [6].

Yet, the potential to fabricate functionally graded or layered ceramic materials - ones that gradually change their composition or microstructure - remains relatively unexplored and underdeveloped. These types of materials can potentially offer a wider range of properties and performance, such as a combination of hardness, toughness, and thermal resistance in a single component, thus expanding the application possibilities for ceramics. Feilden [7], inspired by natural Bouligand structures, used AM techniques to synthesize damage tolerant structures

* Corresponding author.
E-mail address: mameyers@ucsd.edu (M.A. Meyers).

https://doi.org/10.1016/j.apmt.2024.102366
Received 12 March 2024; Received in revised form 16 July 2024; Accepted 27 July 2024
Available online 8 August 2024

Table 1
Ink formulations used for multi-material direct ink writing of ceramic parts.

Ink Type	Ceramic Powder (vol. %)	PEI (vol. %)	HCl (vol. %)	Water (vol.%)	Methylcellulose (vol.%)
SiC	47.50	3.00	–	47.00	2.5
B_4C	47.50	3.79	5.00	38.71	5

consisting of aligned alumina platelets to tune crack propagation and improve toughness. Sintering of multilayered B_4C-SiC composites results in residual stresses from coefficient of thermal expansion mismatch that can increase the effective fracture toughness [8]. Ravichandran [9] developed a residual stress model for material gradients and found that linear gradients result in a minimum residual stress. Multi-material additive manufacturing has the potential to locally tailor mechanical properties and thus failure behavior [10,11]. Many research endeavors in ceramic AM have concentrated on the development of homogeneous materials, and much progress has been made in this regard. Our research seeks to bridge the knowledge gap for multi-material AM of ceramics by focusing on the mechanical characterization of both homogeneous and heterogeneous ceramics fabricated through direct ink writing. By investigating how different fabrication parameters and material configurations influence the mechanical performance, we aim to enhance the understanding and feasibility of AM for ceramic materials.

The damage evolution process for advanced ceramics changes based on loading conditions. In tension, brittle materials fail from the single largest flaw subjected to the maximum tensile load. Conversely, in compression, brittle materials fail due to the coalescence of many microcracks, in the form of 'wing-tip' tension cracks, which results in fragmentation [12–14]. Further, as loading rate changes from quasi-static to dynamic, inertial effects in crack propagation result in higher measured strength [15], toughness [16,17], and hardness [15]. There is a direct competition between the loading rate and flaw propagation velocity that manifests itself at a strain rate above a critical value (approximately 102 s-1 for aluminum nitride [18]). Nemat Nasser and Deng [19] and Ravichandran and Subhash [20] independently developed theoretical frameworks predicting this transition. A critical parameter is the initial flaw density, where strength increases when the loading rate is such that cracks cannot encounter each other. Consistent with this, Suresh et al. [17] found that mode-I fracture toughness increases by 10–30 % for Al_2O_3 and SiC and 40 % for Si_3N_4 when testing strain rate goes from quasi-static to dynamic regimes.

We propose that heterogeneous structuring, through multi-material AM, will unlock extrinsic mechanisms that improve mechanical

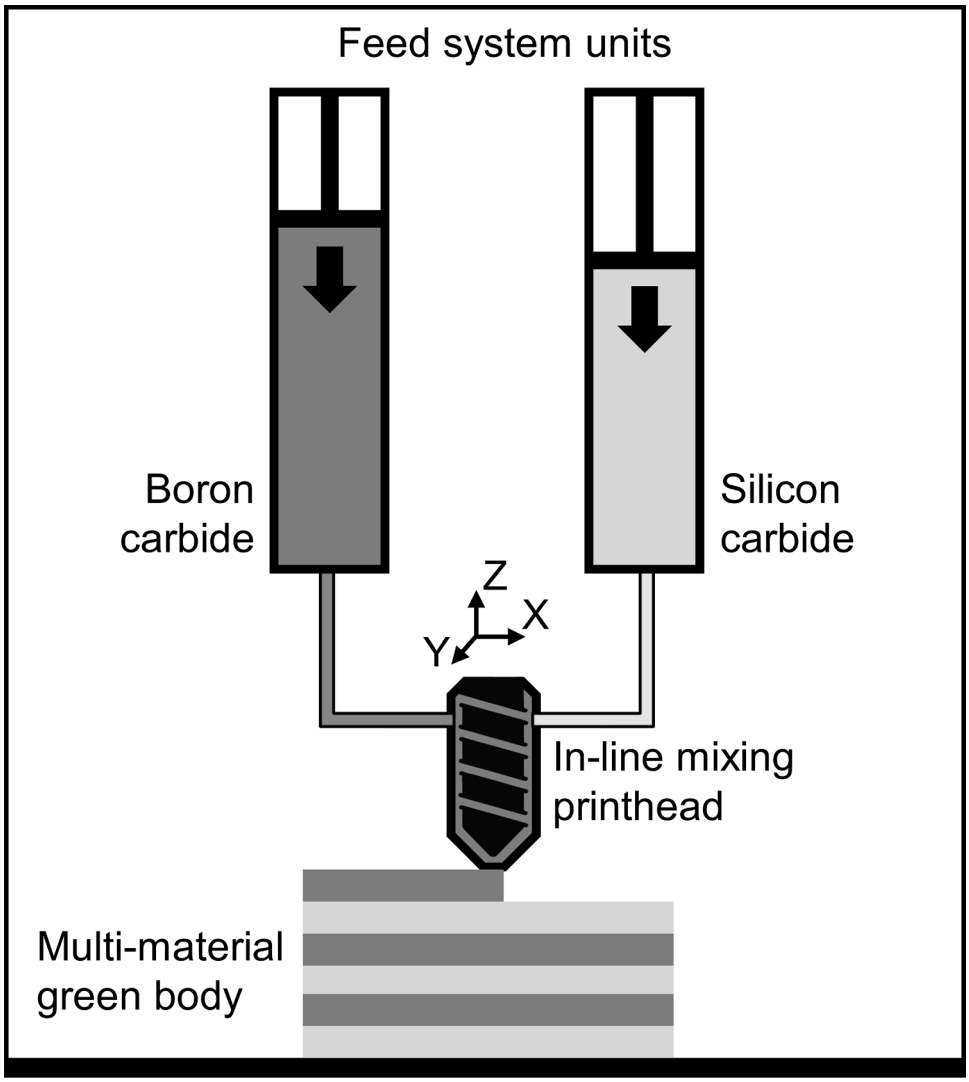

Fig. 1. Schematic of the multi-material direct ink writing system. The system includes two feed system units, a print head, a controller, and a three-axis motion platform. The units are loaded with different ceramic inks and the controller coordinates movement and feed rate, enabling the in-link mixing printhead to spatially tailor composition.

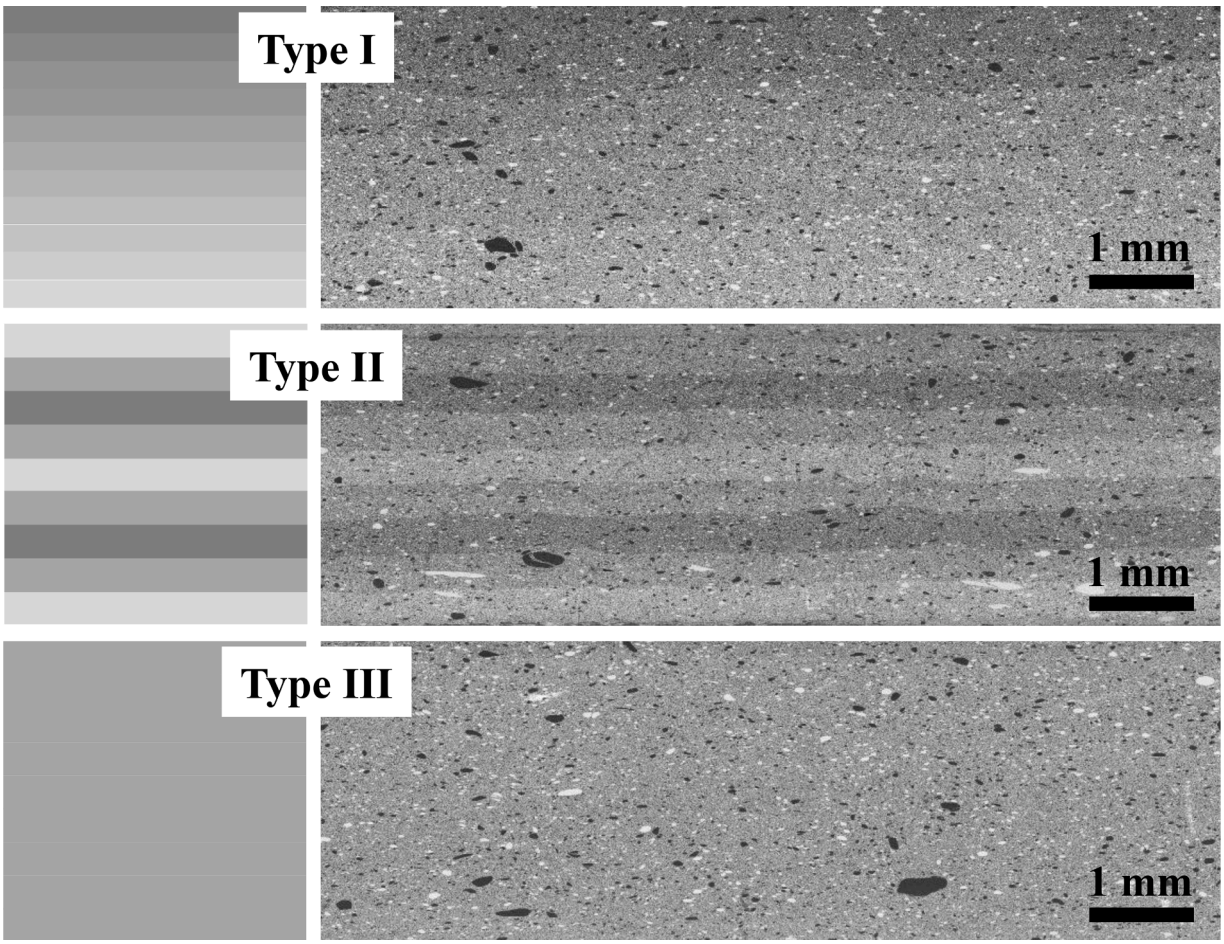

Fig. 2. Carbide ceramic design type diagrams (left) and electron micrographs (right) that were characterized and mechanically tested in this study. The light, medium, and dark shades of gray represent B_4C-SiC mixtures of 60, 50, and 40 vol.% SiC, respectively. For example, the Type-I specimen goes from SiC-rich (60 vol.% SiC) at the bottom to B_4C-rich (40 vol.% SiC) at the top in compositional steps of 2 vol.%. Scanning electron micrographs were captured with an FEI Apreo SEM in backscatter mode to increase phase-contrast.

performance. This study intends to determine the effects of multi-material ceramic AM, specifically functional grading and layering, on the mechanical properties and failure mechanisms of carbide ceramics. Three types of B_4C-SiC specimens, Type-I, Type-II, and Type-III, were produced via multi-material direct ink writing and resulted in mesoscale compositional features. The three design variations were characterized and mechanically tested at quasi-static (10^{-3} s^{-1}) and dynamic (10^{2} s^{-1}) strain rates, with the goal of elucidating structure-property relationships that may improve mechanical performance.

2. Experimental procedures

2.1. Feedstock preparation

Two aqueous carbide inks, one boron carbide and one silicon carbide, were formulated with yield-pseudoplastic behavior for use as the DIW feedstock material. The boron carbide ink consists of 47.5 vol.% B_4C powder (mean particle size ~ 0.8 μm, Hoganas Grade HS, Germany), 3.79 vol.% polyethyleneimine (25 kDa PEI, Sigma-Aldrich, Louis, MO), 5 vol.% hydrochloric acid (96.99 % HCl, Sigma-Aldrich, Louis, MO), 5 vol.% methylcellulose (4000cP MC, Sigma-Aldrich, Louis, MO), and remainder deionized water. The silicon carbide ink contains 47.5 vol.% SiC powder (mean particle size ~ 0.7 μm, Kyocera Grade UF 15, Chicago, IL), 3.00 vol.% polyethyleneimine (25 kDa PEI, Sigma-Aldrich, Louis, MO), 2.5 vol.% methylcellulose (4000cP MC, Sigma-Aldrich, Louis, MO), and remainder deionized water. Ink formulations are described in Table 1.

The inks were homogenized using a DAC 400 VAC SpeedMixer (Flacktek, Landrum, SC). Powder, binders, dispersants, and water were added in steps and mixed thoroughly. In total, three rough mixing stages (up to 1600 rpm) and one final mixing stage (up to 2000 rpm) were used to formulate the carbide inks. Both inks have pseudoplastic (shear thinning) rheological behavior with an appropriate yield stress for DIW processing. The formulation and characterization of the carbide inks used in this study are based on and described thoroughly in previous work by the authors [21].

2.2. Multi-Material direct ink writing

This study builds on previous work by the authors wherein the development of the original multi-material direct ink writing system is detailed [21,22]. Fig. 1 is a schematic of the system, which includes two feed system units, a print head, a controller, and a three-axis motion platform. One unit was loaded with boron carbide ink and the other was loaded with silicon carbide. The controller coordinates movement and feed rate, so that the correct feeding ratio is provided to the print head to tailor the geometry and composition. For example, a Type-I design is printed by incrementally changing the feed ratio (the relative amounts of boron carbide and silicon carbide inks from each feed unit) between two set-points. The print head utilizes an auger to in-line mix and extrude the ceramic ink at any specified ratio in traces, layer-by-layer, to produce a three-dimensional specimen. The print head uses a 15 mm

long alumina tube with an inner diameter of 1.6 mm as the nozzle, printing speed of 12 mm/s, and varying layer height between 0.5–0.75 mm. Green bodies of the desired composition variation (Type-I, Type-II, and Type-III) were printed as 38.1 mm diameter by 10.55 mm height cylindrical disks. The disks were printed on removable acrylic plates that were placed into a sealed container immediately after printing to avoid cracking.

The heterogeneous and homogeneous designs are illustrated in Fig. 2. The Type-I specimen composition varies from SiC-rich (60 vol.% SiC) to B_4C-rich (40 vol.% SiC) in 11 layers with 2 vol.% change per layer. The Type-II specimen has 9 layers that vary from SiC-rich (60 vol.% SiC) on the bottom, middle, and top with B_4C-rich (40 vol.% SiC) regions in between separated by 50 vol.% SiC layers. It is important to note that the Type-II specimen is symmetric in design, while the Type-I specimen is asymmetric. The asymmetric Type-I disks have SiC rich material at the top layer and B_4C rich material at the bottom layer. The Type-III specimen has a homogeneous composition of 50 vol.% SiC and 50 vol.% B_4C throughout.

2.3. Post-processing

All printed samples were dried under controlled humidity (77 % RH) for several days before further processing. The dried samples were pressed in graphite dies under a uniaxial pressure of 35 MPa. For bars and cubes, the green bodies were pressed as printed. For dumbbells, a 50/50 vol.% blend of SiC and B_4C powder was placed above and below the printed sample within the die to allow for enough material to grip during the machining process. Following green pressing, all samples were (1) pyrolyzed by ramping at 1 °C/min up to 650 °C and holding for 6 h under flowing Ar and (2) densified through hot pressing. The specimens were hot pressed at 35 MPa and 1950 °C for 3 h, using a 20 °C/min ramp rate to an intermediate hold at 1300 °C for 1 h to volatilize oxide species such as B_2O_3, and then 10 °C/min up to sintering temp. Samples were cooled at 3 °C/min and the entire process was performed under vacuum. Final, dense specimens were grit blasted to remove graphfoil adhered to the surface from the hot-pressing process. Specimens were ground to a height of 3 mm by a 120-grit diamond grinding wheel and sectioned into bars by a diamond cutting wheel using an automatic surface grinder (Model FSG-3A1020, Chevalier, Santa Fe Springs, CA). Two bars of each specimen type were sectioned into cubes using a low-speed saw (Model 650, South Bay Technology, San Clemente, CA) and hot-pressed diamond blade (MTI Corporation, Richmond, CA) with a 63 μm grit size. All sides of every section were polished to a 15 μm grit size to meet mechanical test sample surface finish requirements. A lapping fixture (South Bay Technologies) was used to hold the cubes during polishing to ensure parallel testing surfaces. The sections used for hardness testing and microstructural characterization were mounted in epoxy and polished following rough and final steps. Rough polishing was accomplished using colloidal diamond suspensions of sizes 30, 9, and 3 μm for times of 30 min, 45 min, and 90 min, respectively. A final polish was done using 1 and 0.25 μm colloidal diamond suspensions for times of 45 and 60 min, respectively. All polishing steps were performed at a 20 N load and with plate and head speeds of 300 and 150 RPM, respectively, in a co-rotating configuration.

The three disks, one of each type, which were sintered with top and bottom caps of 50/50 vol.% B_4C-SiC material to produce disks with 32 mm height and 38.1 mm diameter, were sent to a specialty machine shop (Bomas, Somerville, MA) and machined into dumbbells of approximately 13 mm total length with cylindrical gauge sections of 2.1 mm diameter and 3.175 mm length. This dumbbell geometry has been shown to produce advantageous results for both quasistatic and dynamic compression of advanced ceramic materials [23]. Machining specifications followed those prescribed by the ASTM Standard C1424 for compressive strength testing of advanced ceramics [24].

2.4. Characterization

SEM micrographs were taken of the polished cross-sections and fracture surfaces (FEI Apreo SEM, Hillsboro, OR). ImageJ was used for all measurements, including grain and inclusion size determination, on SEM micrographs [25]. Phase determination was accomplished via x-ray diffraction (XRD). A single cube from each specimen (described in Section 2.3) was milled into powder using a high-energy mill (8000 M Mill, SPEX SamplePrep, Metuchen, NJ). Milling was performed for two minutes in a polycarbonate capsule with two tungsten carbide milling media. Powder was dispersed into a small amount of ethanol, pipetted on to Si XRD sample holders, and allowed to dry, forming thin layers of powder for XRD analysis. Analysis was performed using a Bruker D2 PHASER 2nd-Gen XRD (Fitchburg, WI). The XRD utilized a Cu K-α source generated at 30 kV and 10 mA. Test conditions for the analysis consisted of a 2Θ range of 10–100° with an increment of 0.02° and step time of 1.0 s. Density was determined using the Archimedes method. Densities are reported as a percentage of theoretical density, which was calculated using a rule of mixtures with values of 2.52 g/cc for boron carbide and 3.21 g/cc for silicon carbide [1]. The relative amounts of each phase, used in the rule of mixtures calculation, were determined by quantitative phase analysis from XRD patterns using the Rietveld method.

2.5. Thermal residual stress modeling

To interrogate the stress state within the multi-phase carbide composites that arises due to thermal residual stress during processing it is necessary to consider both the stress between layers at the macroscale, and the stress within the blended layers at the microscale. At the macroscale, the formulations developed by Hsueh et al. [26,27] were utilized, which decomposes the problem into uniform strain and bending strain components. Using this methodology, it is possible to determine the average strain (c), the bending axis (t_b), and the radius of curvature (r), with the following expressions:

$$c = \frac{\sum E'_i t_i \alpha_i \Delta T}{\sum E'_i t_i}$$

$$t_b = \frac{\sum E'_i t_i (2h_{i-1} + t_i)}{2\sum E'_i t_i}$$

$$\frac{1}{r} = \frac{-3\sum E'_i t_i (c - \alpha_i \Delta T)(2h_{i-1} + t_i)}{\sum E'_i t_i \left[6h_{i-1}^2 + 6h_{i-1}t_i + 2t_i^2 - 3t_b(2h_{i-1} + t_i)\right]}$$

where E' is the biaxial modulus of the layer, α the coefficient of thermal expansion of the layer, t the layer thickness, $h_i = \sum_{j=1}^{i} t_j$, and ΔT the change in temperature. The effective coefficient of thermal expansion for a layer is determined by rule of mixture, and the effective biaxial modulus is given by $E' = \frac{E_1 f_1 + E_2 f_2}{1 - \nu_1 f_1 - \nu_2 f_2}$, with ν and f the Poisson's ratio and volume fraction, respectively, of the component materials within the layer. It is then possible to determine the in-plane stress within layers using:

$$\sigma_x = E_i\left(c + \frac{z - t_b}{r} - \alpha_i \Delta T\right)$$

By assuming a traction free boundary condition, the imaginary shear force and moment on the surface, per unit depth, for a cross section at point z_0 in the direction layering can be determined and related to the shear (τ) and normal stress (σ_n):

$$V = \int_{z_0}^{h_n} \sigma_x dz = \int_{R_0}^{R} \tau dx$$

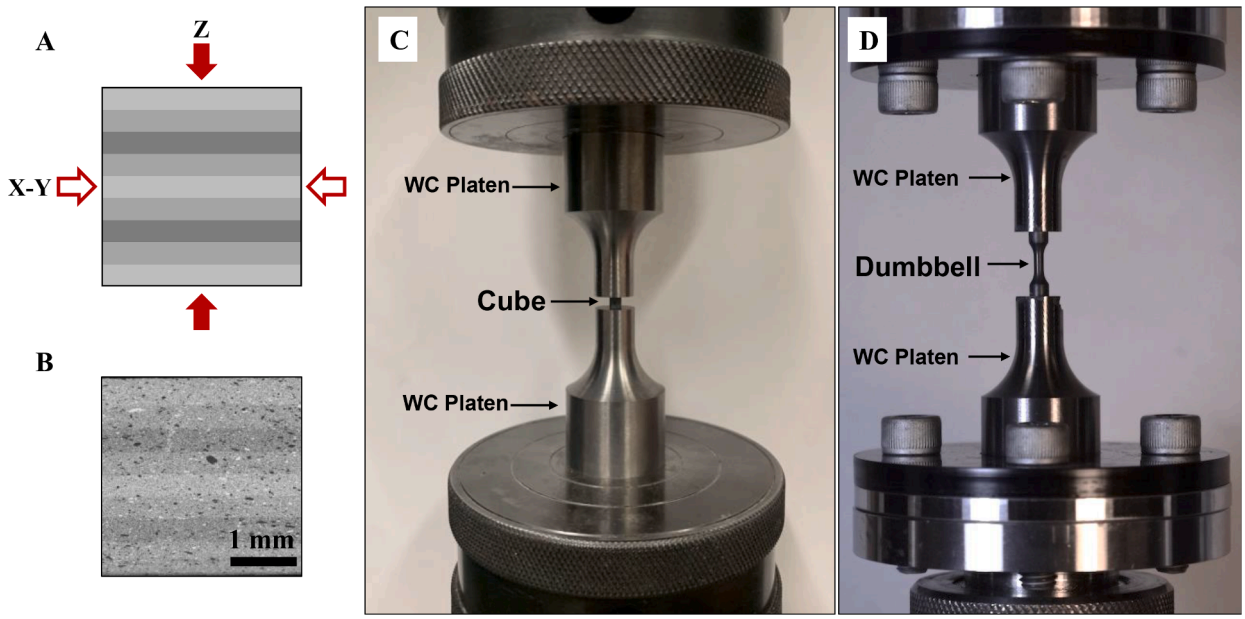

Fig. 3. Carbide cubes were tested in compression at quasi-static (10^{-3} s^{-1}) and dynamic (10^{2} s^{-1}) strain rate regimes in two orientations. A) The Z orientation aligns with the DIW build direction and is normal to layer interfaces, while the X-Y orientation is parallel to layer interfaces. In addition, the Z orientation is parallel to the hot-pressing direction. Arrows show separate loading conditions and are not showing confinement. B) Electron micrograph of a side of a heterogeneous cube with the Type-II design. Tapered tungsten carbide platens were used during quasi-static compression testing for both C) cube and D) dumbbell geometry specimens.

$$M = \int_{z_0}^{h_n} \sigma_x (z - z_0) dz = \int_{R_0}^{R} \sigma_x (x - R_0) dx$$

where R is the radius of the produced carbide specimens and R_0 is the radius at which the shear and normal stresses go to zero, which has been approximated to be $0.7R$ by FEM studies of layered composites [28]. Functional forms for the shear and normal stress within layered composites have been proposed by Bao et al. [29]:

$$\tau = \tau_0 \left(\frac{x - R_0}{R - R_0} \right)^m$$

$$\sigma_n = D\left((x - R_0)^{m-1} - x_0^{m-1} \right)$$

where $x_0 = (R - R_0)\left(\frac{1}{m}\right)^{1/m-1}$ and m is a material constant which for ceramics is generally between 4 and 6. A value of $m = 6$ is used within this work to represent the most extreme case. By combining all the above equations, it is possible to analytically approximate the macroscopic stress any point with only the layer thickness and configuration, part dimensions, Youngs modulus, Poisson's ratio, and coefficient of thermal expansion. The material properties utilized for the B_4C and SiC can be found in Table [30-32].

To account for the stresses at the microscale, Eshelby inclusion theory [33], in conjunction with Mori-Tanaka mean stress theory [34], is utilized. Utilizing these classic formulations, average stress in both the matrix (m) and inclusions (i) of any layer can then be approximated with the following expressions [35]:

$$\bar{\boldsymbol{\sigma}}_m = \frac{1}{1-f}(\boldsymbol{M}_i - \boldsymbol{M}_m)^{-1}(\boldsymbol{M}_i - \boldsymbol{M}_c)\boldsymbol{\sigma}_{app} - \left\{ (\boldsymbol{M}_i - \boldsymbol{M}_m)^{-1}(\boldsymbol{M}_i - \boldsymbol{M}_c) - \boldsymbol{I} \right\} \boldsymbol{M}_m^{-1}(\boldsymbol{I} - \boldsymbol{S})\boldsymbol{\varepsilon}^*$$

$$\bar{\boldsymbol{\sigma}}_i = \frac{1}{1-f}(\boldsymbol{M}_i - \boldsymbol{M}_m)^{-1}(\boldsymbol{M}_c - \boldsymbol{M}_m)\boldsymbol{\sigma}_{app} - \frac{1-f}{f}(\boldsymbol{M}_i - \boldsymbol{M}_m)^{-1}(\boldsymbol{M}_c - \boldsymbol{M}_m)\boldsymbol{M}_m^{-1}(\boldsymbol{I} - \boldsymbol{S})\boldsymbol{\varepsilon}^*$$

where $\boldsymbol{M}$ is the compliance tensor, $\boldsymbol{I}$ is the identity matrix, $\boldsymbol{S}$ is the Eshelby tensor, and f is the volume fraction of the inclusion phase. $\boldsymbol{\varepsilon}^*$ is the strain from the mismatch in thermal expansion coefficients and is given by $\boldsymbol{\varepsilon}^* = (\alpha_i - \alpha_m)\boldsymbol{I}\Delta T$. $\boldsymbol{M}_c$ is the effective compliance of the composite and is given by $\boldsymbol{M}_c = \boldsymbol{M}_m + f\left\{ \left[\boldsymbol{M}_i \boldsymbol{M}_m^{-1} - \boldsymbol{I} \right]^{-1} + (1-f)(\boldsymbol{I} - \boldsymbol{S}) \right\}^{-1} \boldsymbol{M}_m$. Within any layer, the matrix is assumed to be the material with the larger volume fraction, and for the purpose of this study all materials are assumed to be isotropic and all inclusions assumed to be spherical. As a result of these assumptions, no additional information beyond what is needed for the macroscale stress predictions is required.

2.6. Mechanical testing

Quasi-static (hardness, compression, and three-point bending) and dynamic (split-Hopkinson pressure bar compression) mechanical testing was performed on the excised samples for the Type-I, Type-II, and Type-III specimens. Dumbbell and cube geometry specimens were used for quasi-static and dynamic compression.

Knoop indentation hardness testing was performed in two test variations to determine both Knoop hardness and the indentation size effect. Knoop indentation was performed using a Wilson VH3100 automatic hardness tester (Buehler, Lake Bluff, IL). HK2 values were determined following the ASTM Standard C1326–13 [36] at a 19.61 N load, 10 s dwell, and spacing greater than 1.5 times the long-diagonal of the indent. Hardness values were determined on the polished cross-section of each specimen type. Ten valid indents were measured for the Type-III specimen. For the Type-II specimen, 10 valid indents each were measured in the B_4C-rich, 50/50, and SiC-rich layers. For the Type-I specimen, a 5 x 11 grid of indents was made to measure five points each at the centers of all layers that range from 40 to 60 vol.% SiC in increments of 2 vol.%. The indentation size effect was determined for

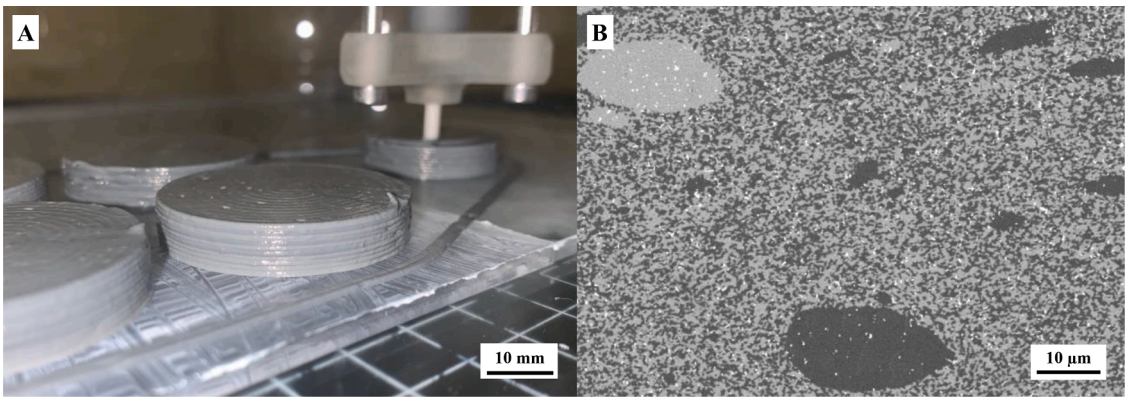

Fig. 4. A) Type-II disks in their green state during the DIW printing process for heterogeneous carbide specimens. B) Electron micrograph of the cross-section of a sintered specimen showing the matrix, composed of particle-scale mixing of the carbide inks, interspersed with larger B_4C and SiC inclusions. Light gray and dark gray materials are SiC and B_4C, respectively, with bright speckles being intergranular porosity.

each specimen using a 10 s dwell and sufficient spacing with loads varying from 0.98 to 19.61 N. Indents were made on the top and bottom polished surfaces of the specimens. A minimum of five valid indents were made for each load.

Flexural strength measurements via three-point bend testing were performed on the excised bars from the carbide disks. Four 3 x 4 x 25 mm bars each were evaluated for Type-III specimens, while eight 3 x 4 x 25 mm bars each were tested for the Type-I and Type-II specimens. The flexural strength ASTM standard for advanced ceramic materials specifies at least 10 bars must be tested and if a 3 mm x 4 mm cross-section is used the outer-span must be 40 mm [37]. Due to processing requirements, a disk height of at least 3 mm was necessary to achieve the desired composition variations. For these reasons, reported flexural strength values will not adhere to ASTM requirements and should only be used for qualitative comparison between heterogeneous and homogeneous designs within this study. A load frame (Universal Testing System 3367, Instron, Norwood, MA) with a 30 kN load cell and displacement control was used for flexural testing. Three-point bend testing was performed at a displacement rate of 0.5 mm/min (strain rate equal to 10^{-4} s^{-1}) with a 20 mm outer-span and 4.5 mm diameter rollers. As the Type-I specimen is SiC-rich at the bottom and B_4C-rich at the top, half of the bars were tested with the SiC-rich side as the tensile surface and visa-versa for the B_4C-rich side. Calculation of the flexural strength, based on the failure load and specimen geometry, followed the method provided by ASTM Standard C1161 for flexural strength of advanced ceramics [37]. Fracture surface analysis was performed using electron microscopy (FEI Apreo SEM, Hillsboro, OR) following procedures and terminology from ASTM Standard C1322 [38].

The compressive strength of the heterogeneous carbide specimens was determined by crushing the cube and dumbbell specimens excised from the printed disks. Load orientation testing was performed using the cube geometry, where six cubes each were tested for X-Y and Z orientations (illustrated in Fig. 3) and specimen type to determine a mean compressive strength. Dumbbell specimens were tested in the z-orientation only, with a sample size of six for each specimen variation, Type-I, Type-II, and Type-III. Quasi-static compression testing was accomplished on a load frame (Universal Testing System 5982, Instron, Norwood, MA) with a 100 kN load cell. For quasi-static compression testing, as shown in Fig. 3C,D, tungsten carbide platens that taper from 25.4 mm to 6.35 mm were used to reduce interfacial stresses that arise due to interactions between the carbide specimens and the more compliant steel compression platens. A displacement rate of 0.5 mm/min was used for quasistatic compression testing, which equates to a strain rate of 2.8×10^{-3} s^{-1}. After failure, fragments were collected to analyze fracture mechanisms via electron microscopy (FEI Apreo SEM, Hillsboro, OR). For dynamic compression testing, strain rates between 100 s^{-1} to 250 s^{-1} were achieved using a split-Hopkinson pressure bar (SHPB). The system consists of Maraging steel incident, transmission, and striker bars of diameter 18.95 mm and length 2 m, 2 m, and 250 mm, respectively. Compressed Ar gas was used to launch the striker bar into the incident bar. The system was aligned using laser-sights; alignment was confirmed by symmetric incident, reflected, and transmitted wave signals for a 'blank' test without any specimen. Strain gauges were mounted at the center of the incident and transmission bars in an active two-leg half-bridge configuration, where both strain gauges are used to actively measure strain, while cancelling out bending stresses. Wheatstone bridge adapters were connected to the strain gauges and connected to signal conditioners (CDV-900A, KYOWA, China) to amplify and condition wave signals. An oscilloscope (GDS-1102A-U, GWINSTEK, Taiwan) was used to record the wave forms. The signal conditioners were used to apply a 100 kHz low-pass filter during measurement to reduce noise. Tungsten carbide platens of diameter 12.7 mm and thickness 6.35 mm, sized to match the impedance of the Maraging steel bars, were placed between the incident and transmission bars and carbide specimen. The platens eliminate unwanted stress concentrations at the specimen edges and corners, in addition to reducing damage to the steel bar ends. A 5.1 mm diameter by 2 mm thick annealed copper disk was placed between the striker and incident bar to ramp the pulse and produce a longer loading time to enable stress equilibrium prior to specimen failure. Post-test, wave forms were analyzed to confirm that both stress equilibrium and constant strain rate conditions were met by the time failure occurred. The compressive strength (σ_c), strain rate ($\dot{\varepsilon}$), and failure strain (ε) were determined based on equations and test validity criteria from Chen and Song [39]. A high-speed camera (Phantom v12.1, New Jersey, USA) was used to collect video of compression tests to determine failure mode and test validity. A frame rate of 41,000/s and exposure of 16 µs were used.

The SHPB can be used to reach strain rates of 10^2 to 10^5 s^{-1}, but for ceramic materials that have a maximum strain at fracture of approximately 1 % in compression a maximum strain rate around 3000 s^{-1} is realistic due to the need to achieve equilibrium [40,41]. Prior to failure, the specimen must reach stress equilibrium and experience a constant strain rate over its entirety [39]. Further, brittle specimens, which are sensitive to stress concentrations, can fail prematurely due to 1) poor flatness or parallelism of the specimen end surfaces, 2) poorly aligned bars, and 3) specimen indentation into the bar ends [39]. For a cylindrical aluminum nitride specimen compressed using a steel SHPB, stress concentrations at the edges were calculated to be 2.7 times the stress at the center of the specimen. This is due to the difference in stiffness between steel and aluminum nitride [42]. For these reasons, Tracy [43] developed dumbbell-type specimens for compression testing of brittle materials. Dumbbell type specimens can be used to reduce end splitting resulting from edge effects and/or lateral tensile stress that can develop

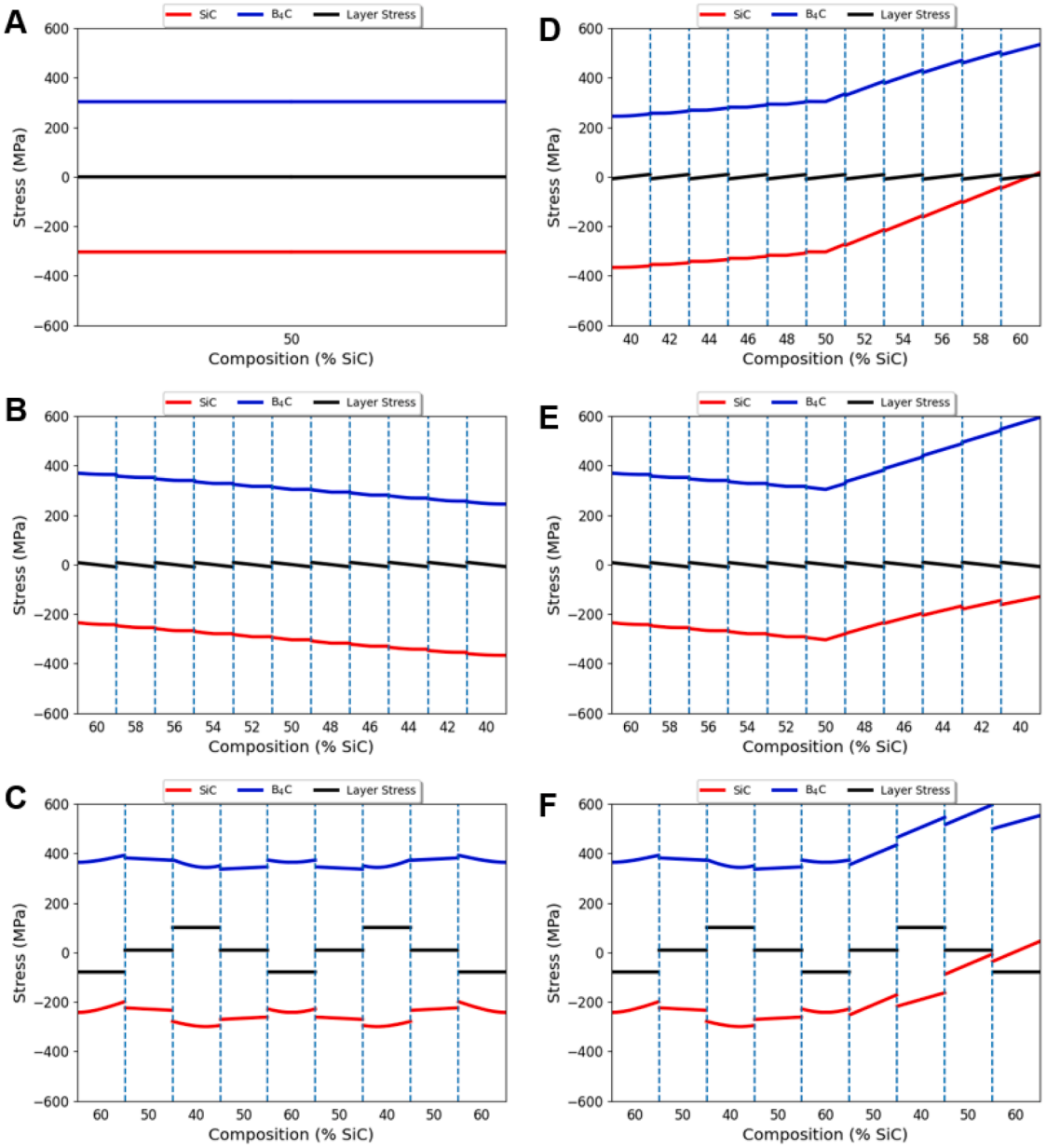

Fig. 5. Residual stress plots for A) Type-III, B) Type-I, and C) Type-II specimen types showing macroscale and microscale residual stress resulting from coefficient of thermal expansion mismatch. Black (layer stress) lines are the macroscale stress state considering the layers to be homogeneous material with properties derived from a rule of mixtures analysis between those of pure B_4C and SiC. Red (SiC) and blue (B_4C) lines demonstrate the microscale stress state where inclusion-matrix residual stress interactions are accounted for. B_4C, with its higher coefficient of thermal expansion, will tend toward tension, while SiC will tend toward compression. The average failure stress state from three-point bend testing is applied to the residual stress plots (right) for D) Type-I-SiC, E) Type-I-B_4C, and F) Type-II specimen types, which showcases the real stress locally throughout each design that causes failure. It should be noted that plot D (Type-I-SiC) has composition reversed so that the testing surface under tensile traction is always on the right side of plots D-F.

at the specimen/loading platen interface for cylinder and cube geometries. An interlaboratory round-robin study confirmed the efficacy of the dumbbell specimen geometry for compression testing of advanced ceramics, specifically alumina [23].

3. Results & discussion

3.1. Microstructural characterization

A printed disk (left) in the green state and typical sintered microstructure (right) is shown in Fig. 4 for the multi-material additively manufactured carbide specimens. Light gray and dark gray components are SiC and B_4C, respectively, with bright speckles being intergranular porosity. The particle scale mixing in the matrix creates a fine mixture of single grains of B_4C and SiC, which surrounds larger inclusions composed of many grains of a single material. This inclusion-matrix structure results in a bimodal distribution of composition at the microscale. Average grain sizes were 0.93 μm (B_4C) and 1.63 μm (SiC). Larger inclusions resulting from agglomerates in the feedstock ink have average diameters of 19.44 μm (B_4C) and 18.92 μm (SiC). For SiC, the largest measured inclusion was 161.81 μm, while the largest B_4C inclusion was 285.47 μm. Likely due to both the direct ink writing and hot-pressing processes, inclusions tend to be elliptical with their long axis parallel to layer interfaces (normal to the hot-pressing direction). Inclusions and agglomerates are essentially localized composition changes at the microscale, and their deviation from the composition of surrounding

Table 2
Material properties for SiC and B_4C utilized in analytical stress predictions. An average value over the considered temperature range is given for α.

	E (GPa)	ν	α (x10^{-6} K^{-1})
SiC	460	0.2	5.28
B_4C	445	0.19	6.11

Table 3
Rietveld quantitative phase analysis results for each printed multi-phase carbide specimen.

Type #	6H (wt%)	15R (wt%)	4H (wt %)	B4C (wt%)	WC (wt%)	SiC (vol%)	B4C (vol%)
Type-I	44.3	1.9	4.8	44.5	4.6	47.5	52.5
Type-II	54.4	1.1	4.0	37.7	2.8	55.3	44.7
Type-III	44.7	2.7	5.3	41.0	6.3	50.2	49.8

material leads to thermally-induced residual stresses that develop from differential shrinkage between inclusions/agglomerates and the matrix material [44,45].

To determine the bulk composition of the Type-I, Type-II, and Type-III specimens, diffraction patterns were analyzed by Rietveld refinement with GSAS-II [46]. Starting values for the lattice constants and atomic positions for the 6-H [47], 15-R [48], and 4H [48] polytypes of silicon carbide along with boron carbide [49] were taken from respective references. The relative amounts of each phase, lattice constants, and sample displacement were refined to achieve weighted R values near 15 % in both cases. Rietveld quantitative phase analysis results are reported in weight-percent in Table 3 and were used to calculate volume-fraction SiC and B_4C. Nominal compositions of the Type-I and Type-III specimens were expected to be 50 vol.% SiC. However, the composition was determined to be 47.5 vol.% SiC (Type-I) and 50.2 vol.% SiC (Type-III). Similarly, the nominal composition of the Type-II design was expected to be 51.1 vol.% SiC, but was measured to be 55.3 vol.% SiC. The observed deviations from nominal composition are likely a consequence of having used inks with imperfectly matched viscosity, which will affect feed rates to the print head and mixing characteristics inside the print head. A small amount of tungsten carbide is present due to the milling process that used tungsten milling media. The volume fraction values are normalized with the tungsten carbide removed. No additional impurities were detected, likely due to the high-purity starting powders. It should be noted that many commercially-available carbide materials, which often utilize lower-grade starting powder, have significant impurity content [50].

3.2. Residual stresses from heterogeneity

The presented thermal residual stress model takes into account both macroscale and microscale residual stresses that arise due to coefficient of thermal expansion mismatch between SiC and B_4C when a component is cooled down from the sintering process to room-temperature. In order to integrate the two models at the different length scales, $\boldsymbol{\sigma}_{app}$ is defined as the stress state predicted at the macroscale. Leveraging the axisymmetric nature of the produced parts, polar coordinates are utilized, with $\sigma_{rr} = \sigma_x$, $\sigma_{zz} = \sigma_n$, and $\sigma_{r\theta} = \tau$. All other stresses are assumed to be zero. As the location of the matrix and inclusion phases within a layer is not known, the average stresses for both are calculated at all points. The principal stresses are then determined at each point and, with the assumption that failure would occur in tension, the maximum value across each cross-sectional plane along the z-axis determined. This model can predict the effect of sintering on specific heterogeneous designs and their thermal residual stress distributions can be readily calculated. The (left) plots in Fig. 5 show macroscale and microscale residual stress resulting from coefficient of thermal expansion mismatch for the A) Type-III, B) Type-I, and C) Type-II specimen types. Black (layer stress) lines are the macroscale in-plane stress state considering the layers to be homogeneous material with properties derived from a rule of mixtures analysis between those of pure B_4C and SiC (presented in Table 2). Red (SiC) and blue (B_4C) lines demonstrate the microscale stress state where inclusion matrix residual stress interactions are accounted for. B_4C, with its higher coefficient of thermal expansion, will tend toward tension, while SiC will tend toward compression. At the macroscale, for the Type-II specimen (Fig. 5C), B_4C-rich layers have a tensile in-plane stress of 100 MPa while SiC-rich layers have a compressive in-plane stress of −80 MPa. The Type-I specimen has a maximum tensile in-plane stress of 10 MPa, an order of magnitude lower. In (right) plots d-F, the average failure stress state from three-point bend testing is applied to D) Type-I-SiC, E) Type-I-B4C, and F) Type-II specimen types to showcase the stress state throughout each

Table 4
Mechanical properties for the Type-I, Type-II, and Type-III specimen variations produced via multi-material AM. Two values of hardness and flexural strength are reported for the Type-I specimen, because these tests were performed separately on the B_4C-rich and SiC-rich sides. A non-standard bend bar geometry was used to determine the *flexural strength.

Specimen	Density [g/cm^3]	Relative Density	Flexural Strength [MPa]	Compressive Strength [GPa]				Knoop Hardness (HK2) [GPa]
				Cube		Dumbbell		
				Quasistatic	Dynamic	Quasistatic	Dynamic	
Type-I-SiC	2.74	94.4 %	*249.6 ± 101.1	2.36 ± 0.56	2.75 ± 0.64	3.96 ± 0.16	5.11 ± 0.47	19.4 ± 0.2
Type-I-B_4C			*360.4 ± 18.2					17.5 ± 0.9
Type-II	2.70	94.2 %	*365.9 ± 72.9	1.77 ± 0.54	2.37 ± 0.77	–	4.33 ± 0.17	18.4 ± 0.5
Type-III	2.70	94.0 %	*281.6 ± 81.3	2.53 ± 0.45	3.68 ± 0.56	–	4.50 ± 0.72	17.0 ± 0.7
CoorsTek PAD SiC-B_4C [CoorsTek.com]	3.05	99.3 %	450	–				26.4
CoorsTek PAD B_4C-SiC [CoorsTek.com]	2.63	98.9 %	320	–				24.5
CoorsTek PAD B_4C [CoorsTek.com]	2.49	98.8 %	450	3.07	–	6.4 ± 0.9	7.0 ± 0.7	25.5
CoorsTek PAD SiC—N [CoorsTek.com]	3.20	99.7 %	570	3.41	–	6.9 ± 0.1	8.6 ± 0.2	23.5
Hot-Pressed Verco B_4C	2.52	100.0 %	392.4 ± 58.4	–				21.7 ± 0.9
Hot-Pressed Verco SiC	3.20	99.7 %	486.9 ± 104.0	–				20.6 ± 0.2
Pressureless SiC-B_4C	2.77	–	–	3.38 ± 0.33	4.28 ± 0.75	–	–	–

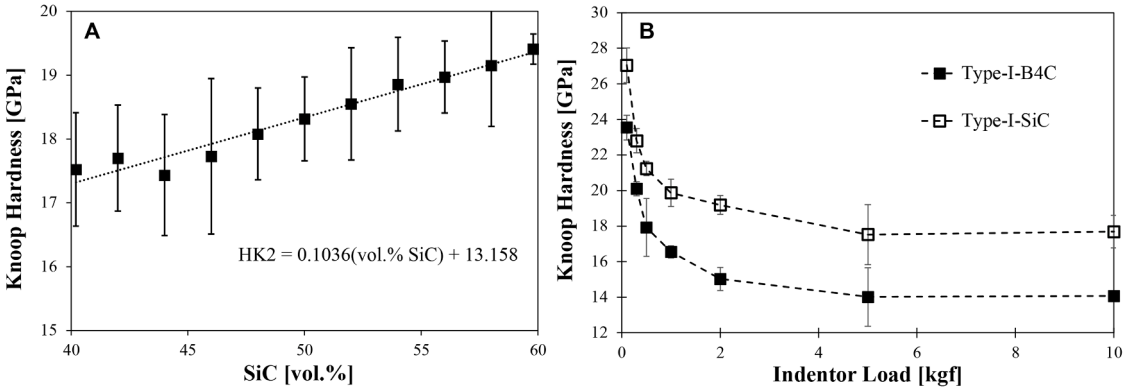

Fig. 6. A) Knoop hardness values measured at a 2 kgf indenter load and 10 s dwell are plotted against volume-fraction SiC for the Type-I specimen. B) Indentation size effect plot for the B_4C-rich and SiC-rich sides of the Type-I specimen.

design that results in failure. It should be noted that plot D (Type-I-SiC) has the composition reversed so that the testing surface under tensile traction during three-point bending is always on the right side of plots d-F.

3.3. Mechanical properties

The hardness, compressive, and flexural strengths were measured to investigate structure-property relationships and failure mechanisms for carbide composites produced via multi-material AM. Knoop hardness measurements were made across layers to test compositional effects and at different loads to determine the effects of residual stress on damage evolution. Compressive strength was tested in quasi-static and dynamic regimes and at orientations perpendicular (Z) and parallel (X-Y) to layer interfaces. Results for quasi-static and dynamic mechanical testing are summarized in Table 4. For reference, mechanical properties reported in the literature and/or the manufacturer's website for boron carbide, silicon carbide, and boron carbide-silicon carbide materials are included. It should be noted that these literature values are from carbides that are at or near full density and that were not processed through additive manufacturing. The final row includes material that was fabricated without pressure-assisted densification.

The flexural strength and Knoop hardness values are reported twice for the Type-I specimen because of it is asymmetric mesostructure, meaning the top is B_4C-rich while the bottom is SiC-rich. Type-I-SiC and Type-I-B_4C flexural strength values represent the flexural strength when the SiC-rich or B_4C-rich side is tensile traction during testing, respectively. Similarly, Knoop hardness values for Type-I-SiC and Type-I-B_4C represent indents made on the SiC-rich or B_4C-rich surface, respectively. The hardness value reported for the Type-II specimen in Table 4 was determined with indents on top surface, which is 60 vol.% SiC. Knoop hardness values for the Type-I specimen are plotted against composition in Fig. 6A, and were calculated based on indents made along specimen cross-sections. Hardness increases with volume-fraction silicon carbide in all cases. The indentation size effect was tested for indenter loads between 0.1–10 kgf for the Type-III, Type-I-SiC, Type-I-B4C, and Type-II specimens. Fig. 6B illustrates the indentation size effect for the B_4C-rich (40 vol.% SiC) and SiC-rich (60 vol.% SiC) sides of the Type-I specimen. Measured hardness decreases with indentation load up to 5 kgf and then becomes load independent. Measured hardness decreases by approximately 40 % from 24 to 28 GPa at 0.1 kgf to 14–18 GPa at 5 kgf. Type-II hardness values closely followed those of the Type-I-SiC across the full indenter load range, which is expected due to both indentation surfaces having a 60 vol.% SiC composition. The Type-III specimen showed the same trend for all indenter loads. At each indenter load, the hardness of the Type-III specimen was lower than the Type-I-SiC and Type-II specimens and greater than the Type-I-B4C specimen, which, again, is expected due to the 50 vol.% SiC composition of the Type-III specimen. These results agree with those reported by Vargas-Gonzalez [1] for hot pressed SiC and B4C materials where measured Knoop hardness drops significantly from 0.5 kgf to 2 kgf. Similar to the Type-I cross-section, measured hardness is lower at all loads for the B4C-rich side of the Type-I specimen. The decreasing measured hardness with volume-fraction B_4C is likely a combined effect from thermally-induced residual tensile stresses and localized porosity (porous regions within large B_4C inclusions have been observed). Hardness data reported for the CoorsTek specimens in Table 4 are significantly higher for two main reasons: 1) Knoop hardness measurements used a 1 kgf indentor load and 2) the density of the CoorsTek materials is roughly 99 % TD compared to the 94 % TD of specimens in this study.

Average flexural values varied between 250 and 350 MPa. The Type-I-SiC specimen tested with the SiC-rich surface in tensile traction (250 ± 101 MPa) had the lowest average flexural strength and greatest standard deviation. The Type-II (366 ± 73 MPa) and Type-I-B_4C (360 ± 18 MPa) specimens showed the highest bending strengths, and the strength of the Type-III specimen (282 ± 81 MPa) fell in between. These trends can be explained in part by differences in the residual stress states present at the surface undergoing tensile traction. Porous regions at the tensile traction surface were the dominate failure mechanism across all types. The difference in flexural strength comes from the effect of mesoscale composition variation on crack propagation. For the specimens that showed high bending strength, the thermal residual stress model predicts that coefficient of thermal expansion mismatch between silicon carbide and boron carbide will result in a compressive stress on the tensile surface (Fig. 5). In order for a crack to propagate, stress at the tensile surface first needs to overcome the compressive residual stress, which increases the bending strength of the Type-II and Type-I-B_4C specimens. The opposite behavior is seen for the Type-I-SiC specimen, where the model predicts residual tensile stresses are present on the surface in tensile traction and, as expected, the flexural strength decreases. A similar relationship has been reported for the effective fracture toughness of ceramic composites that contain thermal residual stresses [8].

Interestingly, if the loading conditions at failure are applied to the model (Fig. 5D-F), the maximum tensile stresses at failure within all carbide specimens are remarkably similar. Plots 4D-F are calculated by superimposing the stress state from three-point bend testing immediately before failure onto the thermal residual stress calculations for each specimen type. The maximum tensile stresses (within B_4C material) at failure are Type-III (582 MPa), Type-II (596 MPa), Type-I-B4C (594 MPa), and Type-I-SiC (533 MPa). The close agreement between the failure stresses, when residual stress is accounted for, supports our hypothesis that residual stress differences due to tailored composition variation was a major contributor to differences in flexural strength. Further, this model may have the potential to predict failure in a variety of ceramic composites, layered, graded, or otherwise. Modelling calculations combined with experimental results indicate that heterogeneous

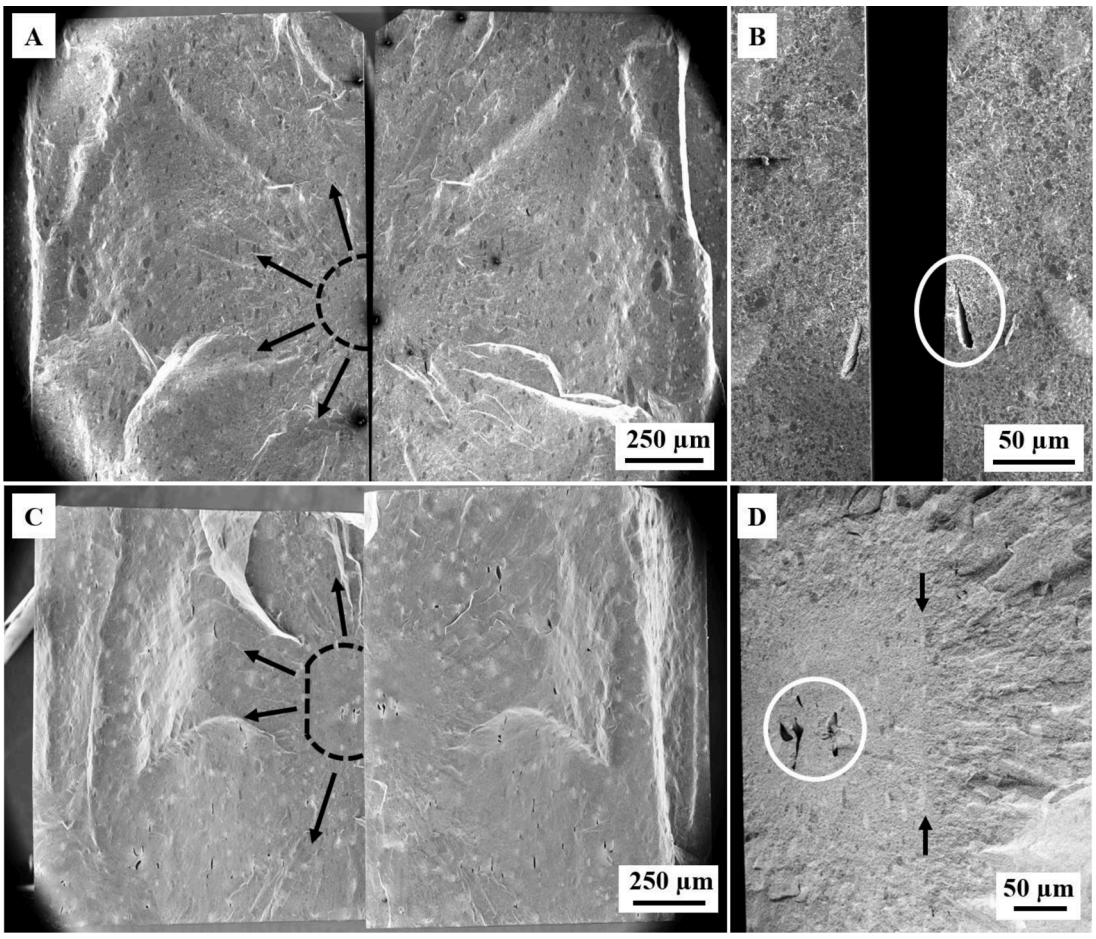

Fig. 7. Fracture surfaces of a A) Type-I bend bar and a C) Type-II bend bar. B) Magnified view of the failure origin for the A) Type-I bend bar. D) Magnified view of the failure origin for the C) Type-II bend bar. The bars are positioned with the tensile testing surface at the center. In both design types, failure originated at large scale porosity (identified with white circles), which formed due to the printing process. Black dotted lines identify the location and morphology of the fracture mirror. Solid black arrows identify the directionality of hackle, which emanate out from the fracture mirror and can be followed in reverse to find the origin of failure.

structuring can significantly affect the flexural strength of a component, even though the failure stress locally within B_4C material stays consistent at approximately 600 MPa. Generally, the theoretical flexural strength of heterogeneous, multi-phase carbides will be lower than monolithic carbides, because thermal mismatch stress within one or more component materials will cause a tensile residual stress state. However, in dynamic applications where the propagation of waves due to ballistic impact generates a highly inhomogeneous stress state, the presence of graded and layered structures may result in improved mechanical performance [52-54]. Predictions from this model may have implications for other measurements of strength properties.

Flexural strength values reported for the CoorsTek materials in Table 4 align with the trends determined in the study. First, as porous regions were the strength limiting feature and often the location of crack initiation, the overall lower flexural strength of specimens fabricated in this study is expected. Second, the monolithic CoorsTek material shows a significantly higher flexural strength as compared to blended B_4C-SiC CoorsTek material, which supports the hypothesis that multi-phase material will fail at lower load during flexural testing due to residual tensile stresses that occur due to coefficient of thermal expansion mismatch.

Surface characterization of the fractured bend bars is presented in Fig. 7 through 9. Representative fracture surfaces of A) Type-I and C) Type-II bend bars are depicted with magnified views of their failure origins presented in B (Type-I) and D (Type-II) are shown in Fig. 7. A circular fracture mirror can be readily identified on the fracture surface of the Type-I-SiC bend bar, Fig. 7A. The mirror region is surrounded by hackle that radiate out from the fracture origin. Inside the mirror at a higher magnification (Fig. 8), cleavage step hackle can be identified running through single grains and is indicative of cracks interacting with the preferred crystallographic orientations in silicon carbide and boron carbide. The failure origin in Fig. 7B can be identified as a pore at the tensile surface, while the failure origin in Fig. 7D is a group of large pores. The fracture mirror for the Type-II specimen in Fig. 7C,D shows an interesting phenomenon where its morphology deviates from circular, with the mirror-hackle transition being aligned parallel to a layer interface. The "flattening" of the fracture mirror is likely due to the interaction with residual stresses, where a change in the stress state influences the development of the mirror and hackle. This change in behavior (compared to the Type-I specimen's circular mirror) appears to be the result of the sharp compositional variation (10 vol.% SiC) in the Type-II specimens compared to the more gradual change in the Type-I specimens (2 vol.% SiC). Electron micrographs of the fracture surface of a Type-II bend bar are shown in Fig. 9 and provide additional examples of how the variations in the composition and mesostructured influence the fracture behavior. Images collected by the backscatter detector (Fig. 9A) and secondary electron detector (Fig. 9B) are superimposed and composited to illustrate these effects. Changes in the fracture behavior are aligned with layer interfaces, where composition variation changes the residual stress state and thus the crack propagation behavior.

The quasi-static (10^{-3} s^{-1}) and dynamic (10^{2} s^{-1}) compressive strength of the 3 mm x 3 mm x 3 mm heterogeneous carbide cubes is presented in Fig. 10 with respect to load orientation. The compressive

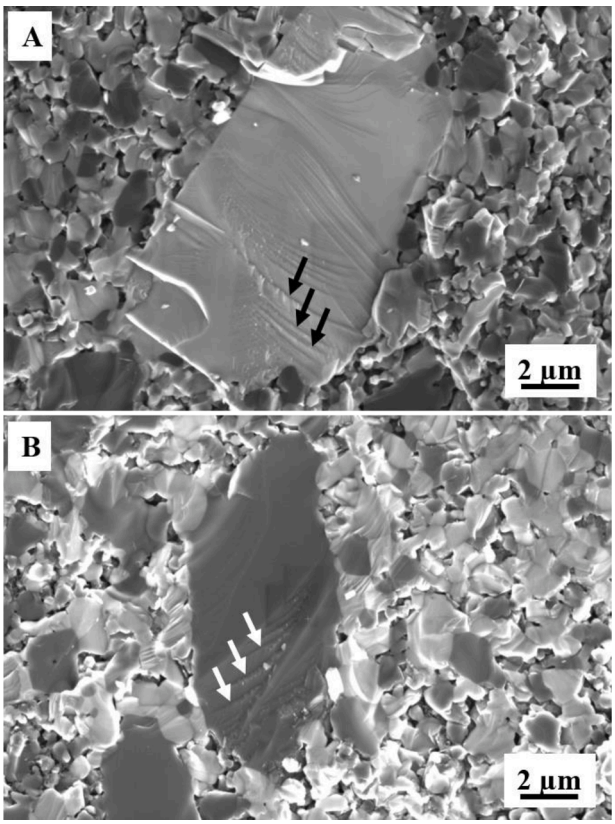

Fig. 8. Cleavage step hackle lines show an interaction between fracture propagation and the preferred crystallographic orientations in large grains of A) SiC and B) B_4C. Black and white arrows identify several adjacent cleavage steps in SiC and B_4C grains, respectively. These micrographs are located within the fracture mirror region of fractured bend bars.

strength appears to be strain-rate dependent with a higher average compressive strength for both orientations under dynamic loading. The significant standard deviation associated with all four data sets makes it impossible to conclusively state that the compressive strength is strain rate dependent. However, this trend is consistent across different subgroupings including by orientation or heterogeneous design type and agrees with results reported by Pittari et al. [15] where the compressive strength of SiC-B4C cuboids was found to be strain rate dependent.

The compressive strength of all specimens was found to be orientation independent. This is different than the results reported by Farbaniec et al. [55], where an orientation effect on the compressive strength of hot-pressed boron carbide was observed. They hypothesized that hot pressing driven texturing of free-carbon rich inclusions (where the long axis of these inclusions aligned normal to hot pressing direction)

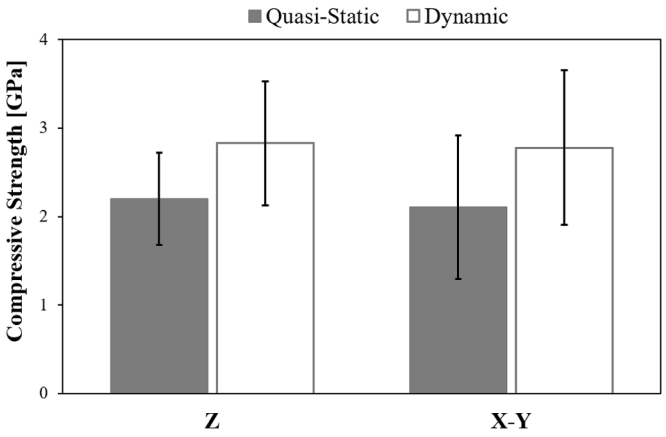

Fig. 10. Mean compressive strength of composite carbide cube specimens with respect to load-orientation for quasi-static (10^{-3} s^{-1}) and dynamic (10^{2} s^{-1}) strain rates.

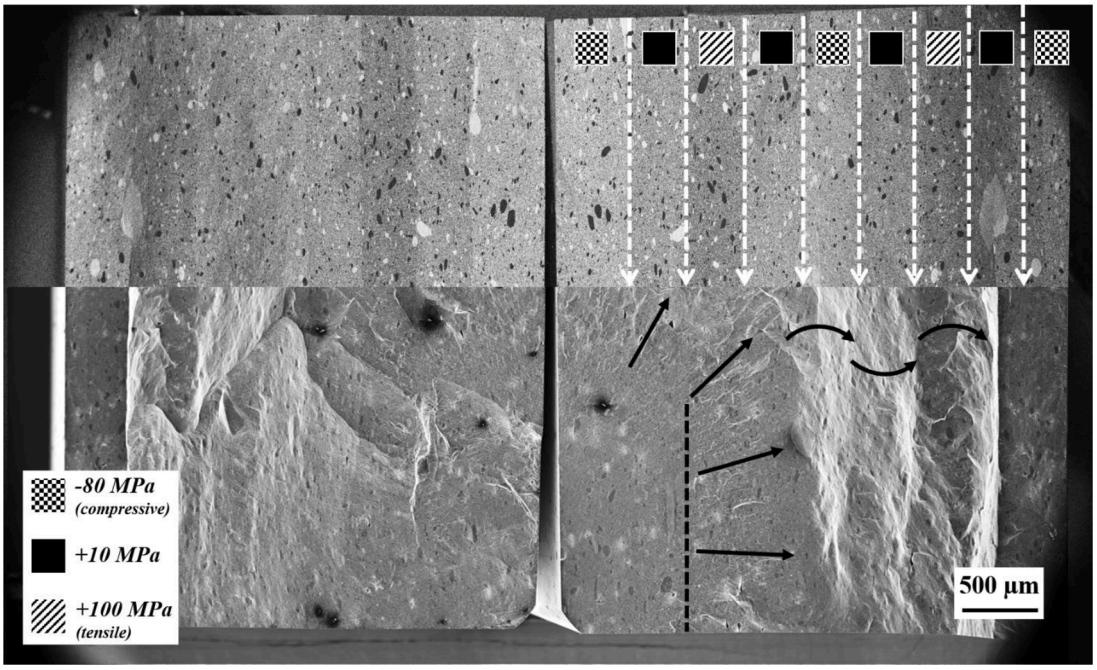

Fig. 9. Fracture surface of a single Type-II bend bar as a composite between (top) backscatter and (bottom) secondary electron microscopy, which shows that the fracture steps align with layer interfaces, where discrete composition changes occur. The mirror boundary, hackle, and fracture steps are identified by black arrows on the secondary electron image, while the layer interfaces are identified by white arrows on the backscatter image. At the macroscale, in terms of the thermal residual stress model, the checkered squares identify layers with an in-plane compressive stress of 80 MPa, solid squares identify layers with an in-plane tensile stress of 10 MPa, and diagonal-striped squares identify layers with an in-plane tensile stress of 100 MPa.

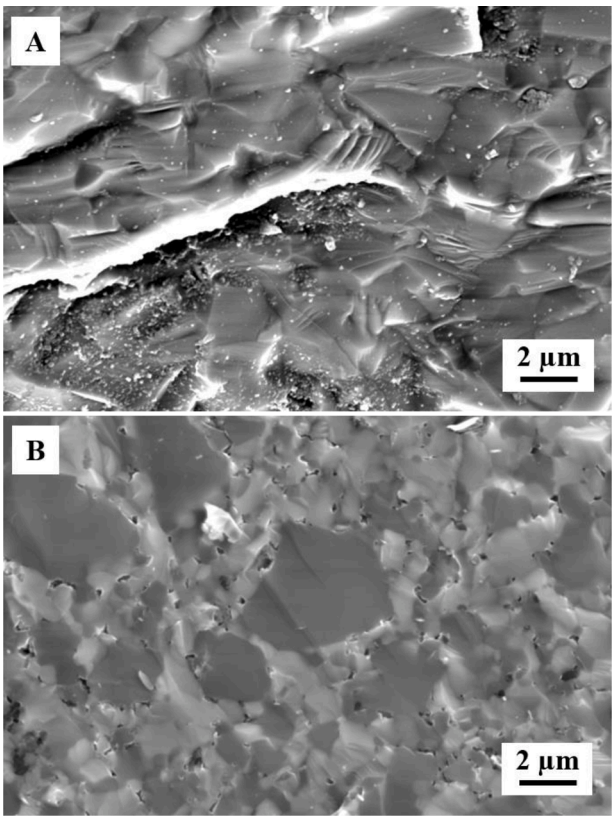

Fig. 11. Fracture surfaces of fragments from (a) quasi-static and (b) dynamic compression testing of heterogeneous carbide cubes. A) A mixed-mode transgranular and intergranular fracture behavior was observed for quasi-static compression test specimens. B) Transgranular fracture was observed to be the dominant behavior during dynamic compression testing.

resulted in a lower compressive strength because microscale sliding occurs preferentially at the flake-like carbon inclusions leading to wing crack growth. The load-orientation independent compressive strength finding in this study is likely due to the B_4C and SiC inclusions in the heterogeneous carbide cubes being more intimately bonded to the matrix than the free-carbon rich inclusions, which could minimize the development and growth of wing cracks. Further, throughout all microstructural analysis, no microcracking around microstructural features, such as large SiC or B_4C inclusions, was observed, supporting the hypothesis that these inclusions are intimately bonded to the matrix. SEM analysis of fragments in Fig. 11 shows that transgranular fracture dominates in dynamic compressive failure, while quasi-static compressive failure leads to mixed-mode transgranular and intergranular fracture behavior.

The compressive strengths of cube and dumbbell geometry Type-I carbide specimens versus strain rate are plotted in Fig. 12. Unlike the data from the cuboids, the dumbbell generated compressive strength values have a tighter standard deviation and show a clear strain-rate dependence. The difference in values for the two geometries is not surprising studies, such as from Swab et al. [51], have shown significant and similar differences in the compression strength of ceramics when dumbbell specimens are used compared to cuboids or cylinders [56–58]. The strain rate dependence of compressive strength in ceramic materials is due to a transition from crack propagation velocity much higher than the load increase to inertia-dominated crack propagation: at high strain rates, the time it takes for cracks to grow and ultimately coalesce is on the same order of magnitude or larger than the load application time.

There is a clear difference in the failure process of these two specimen geometries as shown in Fig. 13. Failure of the cuboids is due to the formation and propagation of macrocracks that run parallel to the loading direction. These macrocracks initiate at the interface of the specimen and the loading platen due to the well documented lateral tensile stresses that develop at this location and are not a true manifestation of a compressive failure mode [59–61]. This failure is typically described as “axial splitting” but the proper term should be “end splitting” to differentiate from the axial splitting described by Horii and Nemat-Nassar [62] in the wing-crack theory that they proposed. The axial splitting they describe results from the initiation and growth of

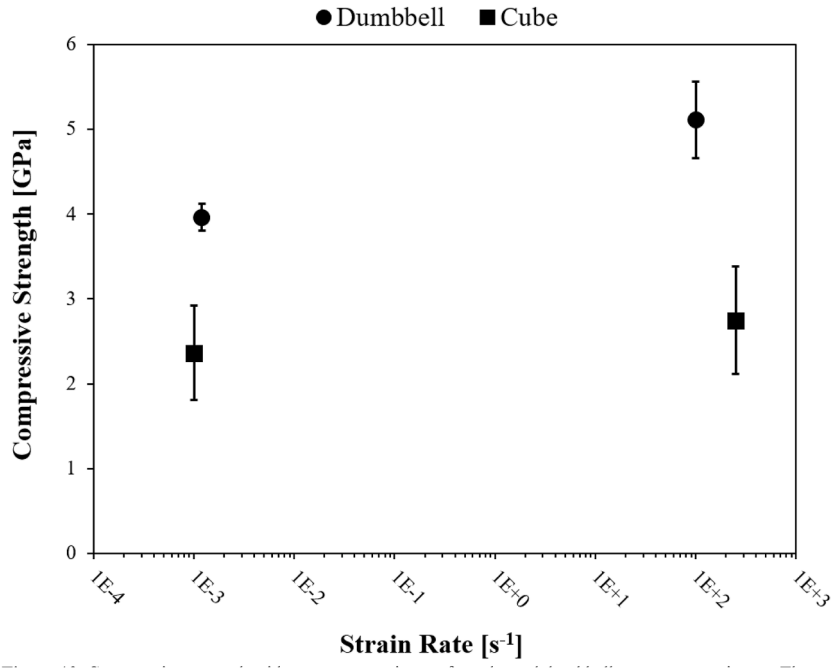

Fig. 12. Compressive strength with respect to strain rate for cube and dumbbell geometry specimens. The compressive strength of dumbbell geometry specimens has a higher strain rate dependence than cube specimens.

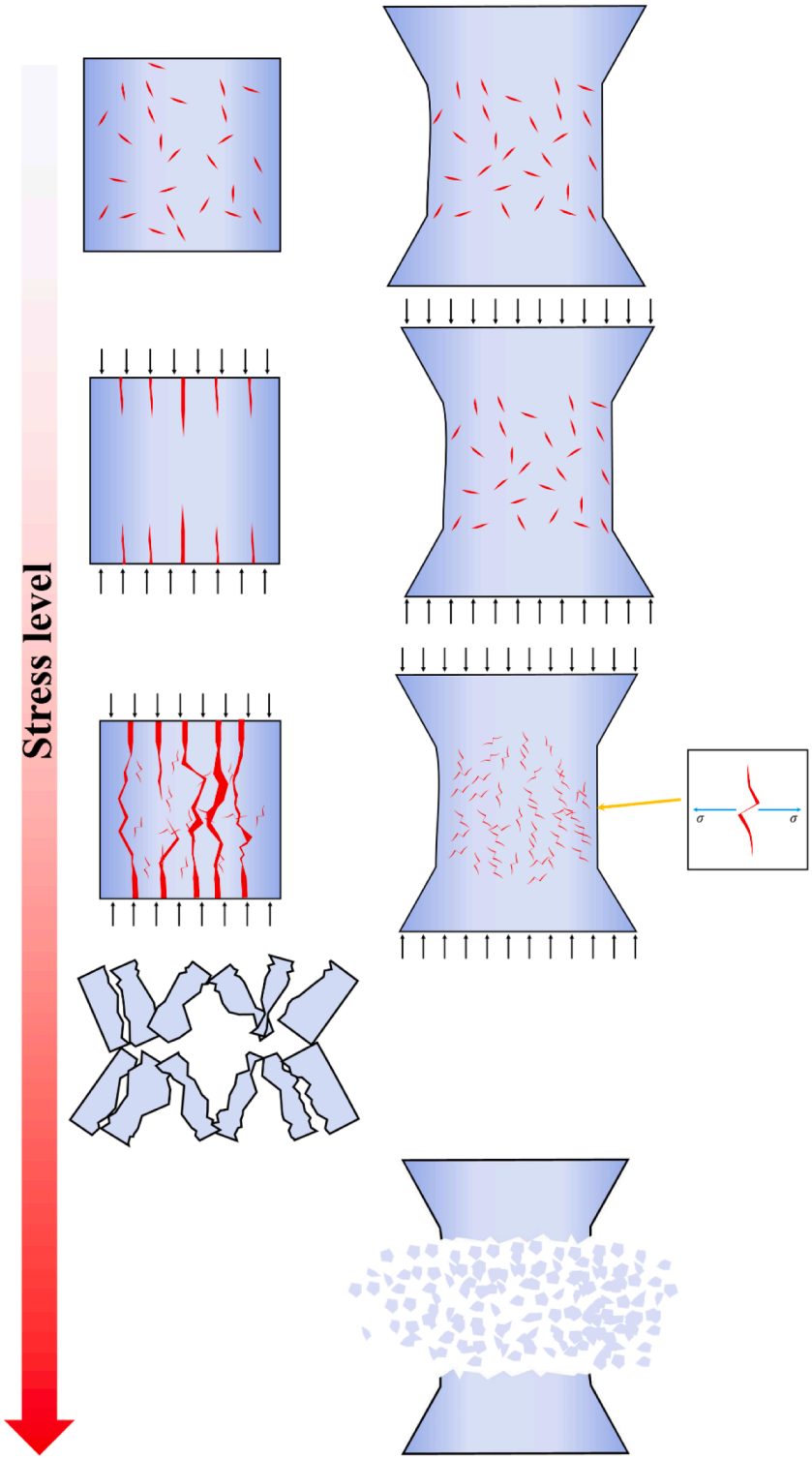

Fig. 13. Sequence of crack generation and growth as a function of compressive stress increase for cube and dumbbell specimens, resulting in significant differences in fragmentation and failure stress. Top: microstructural features that existing in the ceramic; middle: difference in crack growth for the two configurations; macrocracks initiating at the end of the cube and microcracks from microstructural features in the dumbbell bottom: activation of axial macrocracks in cubical specimen and microcracks in dumbbell specimen leading to significant differences in fragmentation process.

microcracks from features in the bulk of the material and not at the ends of the specimens. On the other hand, failure of the dumbbell specimen occurs in the highly stressed gage section by the initiation, growth and coalescence of microcracks as described by Horii and Nemat-Nasser [12, 62]. This type of failure is a true manifestation of a compressive failure in ceramics.

This effect can explain the difference in strain-rate dependence between cube and dumbbell geometry specimens: the failure mode of the cube specimens, as seen in Fig. 14, was not through microcrack growth and coalescence, but instead through end splitting due to lateral tensile stress concentrations at the specimen-platen interface. These tensile stress concentrations create a few major cracks that propagate the length

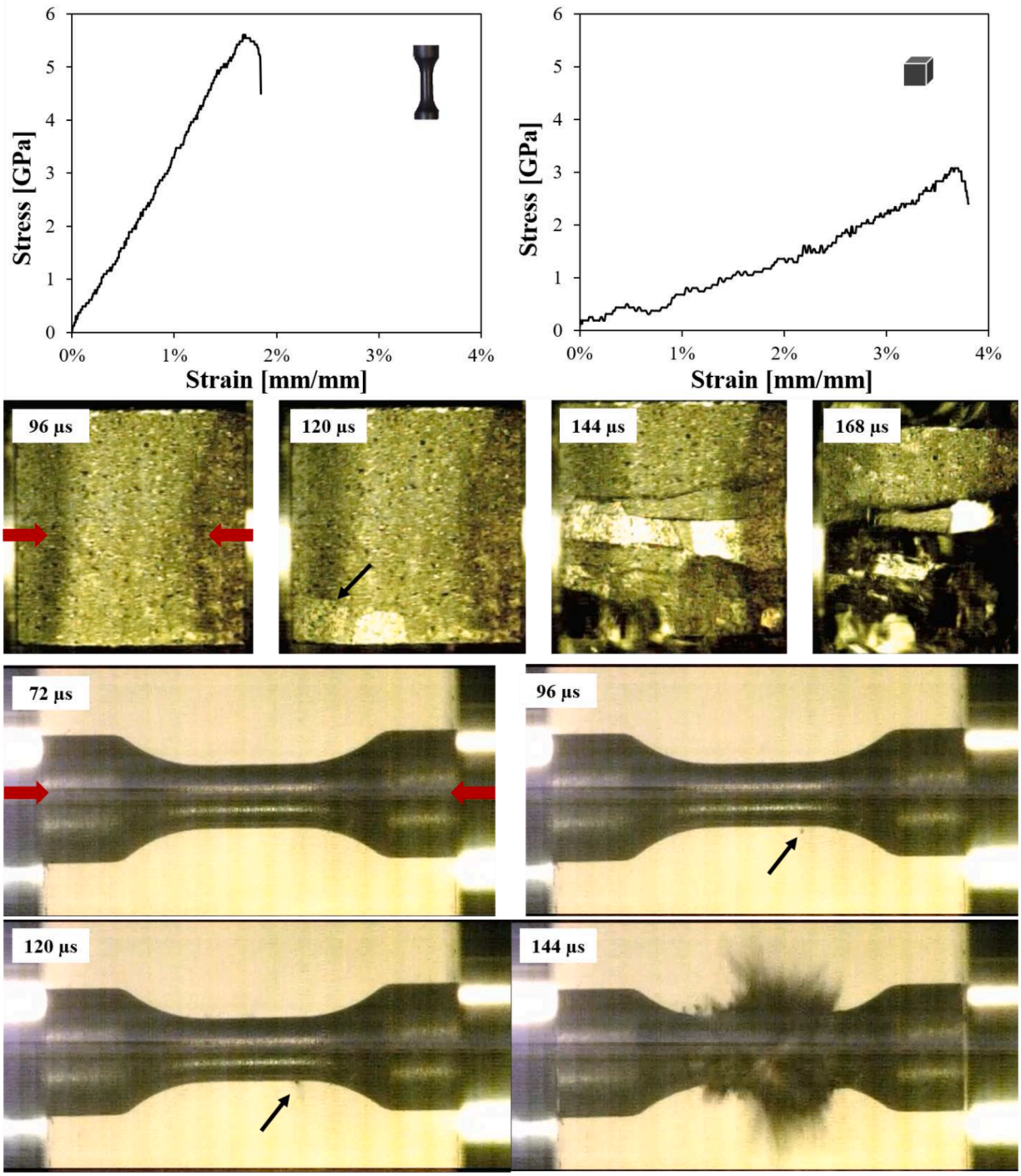

Fig. 14. Stress-strain plots for dynamic (10^2 s^{-1}) compression by split-Hopkinson pressure bar of dumbbell (left) and cube (right) shaped heterogeneous carbide specimens. Both specimens were Type-I type and tested in Z-orientation with layers perpendicular to loading direction. Loading orientation is from left to right (red arrows), with the incident wave coming from the left. A high-speed camera (Phantom v12.1, New Jersey, USA) was used to collect video of compression tests to determine failure mode and test validity. A frame rate of 41,000/s and exposure of 16 µs were used. Four consecutive frames for each specimen geometry are shown labelled with the time since the incident wave reached the left side of the carbide specimen. A black arrow identifies the observed origin of failure that is located within the gauge section.

of the entire specimen and are aligned with the loading direction.

The contrast between dominant failure modes for dumbbell and cube geometry specimens can be observed in Fig. 14, where failure originates at the specimen-platen interface for cubes versus within the gauge section of the dumbbell specimens. The compressive strength of the heterogeneous carbide dumbbell geometry is greater for both quasi-static (68 %) and dynamic (86 %) strain rates than the cube geometry specimens. The dumbbell specimens have a significantly higher compressive strength, because failure occurs due to microcrack generation, growth, and coalescence. This finding is supported by the literature where cubes and dumbbells of identical material (PAD B_4C) were tested at quasi-static and dynamic strain-rates and similar trends in compressive strength were reported [55,63]. Fig. 14 shows stress-strain plots for dynamic (10^2 s-1) compression by split-Hopkinson pressure bar of dumbbell (left) and cube (right) shaped heterogeneous carbide specimens. Both specimens are of the Type-I and tested in Z-orientation with

layers perpendicular to loading direction. Loading orientation is from left to right, with the incident wave coming from the left, indicated by arrows. Four consecutive frames from the high-speed camera (Phantom v12.1, New Jersey, USA) for each specimen geometry are shown labelled with the time since the incident wave reached the left side of the carbide specimen.

4. Conclusions

The feasibility of producing structural, heterogeneous ceramics by additive manufacturing is demonstrated. The following are the principal conclusions drawn from this investigation:

- The composition variation (heterogeneity) led to thermal residual stresses. A multi-scale model was developed for the calculation of thermal residual stresses. One interesting finding being that they are an order of magnitude lower in the Type-I structure compared to the Type-II structure.
- Flexural strength is dependent on the residual stress state of the testing surface under tensile traction. For a compressive residual stress state, flexural strength increased, while for a residual tensile stress state the flexural strength decreased and the standard deviation increased. The Type-II bend bars had the highest mean flexural strength of 366 MPa, which is believed to be due to thermally-induced compressive residual stresses in the surface layers.
- Compressive strength was found to be load-orientation and composition-variation independent. Compressive strength values obtained using the dumbbell-shaped specimen were consistently higher than those obtained from cuboids. Type-I dumbbells had the highest mean compressive strengths of 3.96 GPa (quasi-static, strain rate of 10^{-3} s^{-1}) and 5.11 GPa (dynamic, strain rate of 10^{2} s^{-1}).
- High-speed video analysis indicates that dumbbell geometry specimens failed due to microcrack growth and coalescence, while cubes failed by end splitting due to the formation of macrocracks that initiated at the specimen/load platen interface.

Statement of significance

We elucidate some new aspects of the flight feathers of birds. These design principles are then used, through additive manufacturing, to create beams that have an improved flexural strength with only a minimal weight penalty. The effect of the foam core, found in the shaft of flight feathers of birds, is also demonstrated to improve the performance by finite element analysis, corroborating the experiments in bioinspired beams.

CRediT authorship contribution statement

Joshua Pelz: Conceptualization. **Nicholas Ku:** Formal analysis. **Taylor Shoulders:** Investigation. **Matthew Guziewski:** Project administration. **Samuel Figueroa:** Investigation. **Jeffrey J. Swab:** Formal analysis. **Lionel R. Vargas-Gonzalez:** Project administration. **Marc A. Meyers:** Project administration, Conceptualization.

Declaration of competing interest

The authors declare that they have no known competing financial interests or personal relationships that could have appeared to influence the work reported in this paper.

Data availability

No data was used for the research described in the article.

Acknowledgements

The authors would like to thank the members of the U.S. DEVCOM Army Research Laboratory, Aberdeen Proving Grounds, MD, specifically Dr. Christopher Meredith and Tucker Moore, for their technical advice, as well as Doug Harris on machining of test specimens. The authors want to acknowledge Aomin Huang, a member of the Meyers group at UCSD, for his technical advice regarding dynamic compression testing using the split-Hopkinson pressure bar. This research was sponsored by the U. S. Army Combat Capabilities Development Command Army Research Laboratory and was accomplished under Cooperative Agreement Number W911NF-19-2-0054. The views and conclusions contained in this document are those of the authors and should not be interpreted as representing the official policies, either expressed or implied, of the CCDC Army Research Laboratory or the U.S. Government. The U.S. Government is authorized to reproduce and distribute reprints for Government purposes notwithstanding any copyright notation herein. Funding was supplemented by the UCSD Center for High Energy Density Science (UCOP LAB FEES GRANT ID: LFR-17-449059). This work was performed in part at the San Diego Nanotechnology infrastructure (SDNI) of UCSD, a member of the National Nanotechnology Coordinated infrastructure (NNCI), which is supported by the National Science Foundation (Grant ECCS-2025752).

Supplementary materials

Supplementary material associated with this article can be found, in the online version, at doi:10.1016/j.apmt.2024.102366.

References

[1] L. Vargas-Gonzalez, R.F. Speyer, J. Campbell, Flexural strength, fracture toughness, and hardness of silicon carbide and boron carbide armor ceramics, Int. J. Appl. Ceram. Technol. 7 (2010) 643–651, https://doi.org/10.1111/j.1744-7402.2010.02501.x.
[2] W.J. Costakis, C. Wyckoff, A. Schlup, M. Wallace, T. Craigs, E. Malek, A. Hilmas, L. Rueschhoff, Material extrusion of highly-loaded silicon nitride aqueous inks for solid infilled structures, Addit. Manuf. 64 (2023) 103425, https://doi.org/10.1016/J.ADDMA.2023.103425.
[3] S. Eqtesadi, A. Motealleh, F.H. Perera, P. Miranda, A. Pajares, R. Wendelbo, F. Guiberteau, A.L. Ortiz, Fabricating geometrically-complex B4C ceramic components by robocasting and pressureless spark plasma sintering, Scr. Mater. 145 (2018) 14–18, https://doi.org/10.1016/j.scriptamat.2017.10.001.
[4] A. Ghazanfari, W. Li, M. Leu, J. Watts, G. Hilmas, Mechanical characterization of parts produced by ceramic on-demand extrusion process, Int. J. Appl. Ceram. Technol. 14 (2017) 486–494, https://doi.org/10.1111/ijac.12665.
[5] I.G. Crouch, Body armour – New materials, new systems, Defence Technology 15 (2019), https://doi.org/10.1016/j.dt.2019.02.002.
[6] M.A. Meyers, Dynamic Behavior of Materials, 1994, https://doi.org/10.1002/9780470172278.
[7] E. Feilden, C. Ferraro, Q. Zhang, E. García-Tuñón, E. D'Elia, F. Giuliani, L. Vandeperre, E. Saiz, 3D printing bioinspired ceramic composites, Sci. Rep. (2017), https://doi.org/10.1038/s41598-017-14236-9.
[8] O.R. Orlovskaya, Nina, M. Lugovy, V. Subbotin, Design And Manufacturing B4c-Sic layered ceramics for armor applications, Ceram. Armor Armor Syst. (2003), https://doi.org/10.1002/9781118406793.ch5.
[9] K.S. Ravichandran, Thermal residual stresses in a functionally graded material system, Mater. Sci. Eng. A 201 (1995), https://doi.org/10.1016/0921-5093(95)09773-2.
[10] S. Hasanov, S. Alkunte, M. Rajeshirke, A. Gupta, O. Huseynov, I. Fidan, F. Alifui-Segbaya, A. Rennie, Review on additive manufacturing of multi-material parts: progress and challenges, J. Manuf. Mater. Process. 6 (2022), https://doi.org/10.3390/jmmp6010004.
[11] A. Nazir, O. Gokcekaya, K. Md Masum Billah, O. Ertugrul, J. Jiang, J. Sun, S. Hussain, Multi-material additive manufacturing: a systematic review of design, properties, applications, challenges, and 3D printing of materials and cellular metamaterials, Mater. Des. 226 (2023), https://doi.org/10.1016/j.matdes.2023.111661.
[12] H. Horii, S. Nemat-Nasser, Compression-induced microcrack growth in brittle solids: axial splitting and shear failure, J. Geophys. Res. 90 (1985), https://doi.org/10.1029/jb090ib04p03105.
[13] M.F. Ashby, S.D. Hallam (Née Cooksley), The failure of brittle solids containing small cracks under compressive stress states, Acta Metallurgica 34 (1986), https://doi.org/10.1016/0001-6160(86)90086-6.
[14] B. Paliwal, K.T. Ramesh, An interacting micro-crack damage model for failure of brittle materials under compression, J. Mech. Phys. Solids. 56 (2008), https://doi.org/10.1016/j.jmps.2007.06.012.

[15] J. Pittari, G. Subhash, A. Trachet, J. Zheng, V. Halls, P. Karandikar, The rate-dependent response of pressureless-sintered and reaction-bonded silicon carbide-based ceramics, Int. J. Appl. Ceram. Technol. 12 (2015) E207–E216, https://doi.org/10.1111/IJAC.12332.

[16] J. Pittari, G. Subhash, J. Zheng, V. Halls, P. Jannotti, The rate-dependent fracture toughness of silicon carbide- and boron carbide-based ceramics, J. Eur. Ceram. Soc. 35 (2015) 4411–4422, https://doi.org/10.1016/J.JEURCERAMSOC.2015.08.027.

[17] S. Suresh, T. Nakamura, Y. Yeshurun, K.-H Yang, J. Duffy, Tensile fracture toughness of ceramic materials: effects of dynamic loading and elevated temperatures, J. Am. Ceram. Soc. 73 (1990), https://doi.org/10.1111/j.1151-2916.1990.tb07613.x.

[18] G. Subhash, G. Ravichandran, Mechanical behaviour of a hot pressed aluminum nitride under uniaxial compression, J. Mater. Sci. 33 (1998), https://doi.org/10.1023/A:1004325926287.

[19] S. Nemat-Nasser, H. Deng, Strain-rate effect on brittle failure in compression, Acta Metallurgica Et Materialia 42 (1994), https://doi.org/10.1016/0956-7151(94)90295-X.

[20] G. Ravichandran, G. Subhash, A micromechanical model for high strain rate behavior of ceramics, Int. J. Solids. Struct. 32 (1995) 2627–2646, https://doi.org/10.1016/0020-7683(94)00286-6.

[21] J.S. Pelz, N. Ku, W.T. Shoulders, M.A. Meyers, L.R. Vargas-Gonzalez, Multi-material Additive Manufacturing of Functionally Graded Carbide Ceramics Via active, In-Line Mixing, Addit Manuf, 2020, https://doi.org/10.1016/j.addma.2020.101647.

[22] J. Pelz, N. Ku, M. Meyers, L. Vargas-Gonzalez, Additive Manufacturing Utilizing a Novel In - Line Mixing System for Design of Functionally Graded Ceramic Composites, 2019.

[23] J.J. Swab, W. Chen, J. Hogan, H. Liao, C. Lo, S. Mates, C. Meredith, J.J. Pittari, R. Rhorer, G.D. Quinn, Dynamic compression strength of ceramics: what was learned from an interlaboratory round robin exercise? J. Dyn. Behav. Mater. 7 (2021) https://doi.org/10.1007/s40870-020-00264-6.

[24] ASTM Standard C1424-15, Standard Test Method For Monotonic Compressive Strength of Advanced Ceramics At Ambient Temperature, ASTM International, West Conshohocken, PA, 2019, https://doi.org/10.1520/C1424-15R19. www.astm.org, 2015.

[25] C.A. Schneider, W.S. Rasband, K.W. Eliceiri, NIH Image to ImageJ: 25 years of image analysis, Nat. Methods (2012), https://doi.org/10.1038/nmeth.2089.

[26] C.H. Hsueh, C.R. Luttrell, S. Lee, T.C. Wu, H.Y. Lin, Interfacial peeling moments and shear forces at free edges of multilayers subjected to thermal stresses, J. Am. Ceram. Soc. 89 (2006), https://doi.org/10.1111/j.1551-2916.2006.00924.x.

[27] C.H. Hsueh, Thermal stresses in elastic multilayer systems, Thin Solid Films 418 (2002), https://doi.org/10.1016/S0040-6090(02)00699-5.

[28] K.P. Wang, Y.Y. Huang, A. Chandra, K.X. Hu, Interfacial shear stress, peeling stress, and die cracking stress in trilayer electronic assemblies, IEEE Transactions on Components and Packaging Technologies 23 (2000), https://doi.org/10.1109/6144.846769.

[29] Y. Bao, S. Su, J.L. Huang, An uneven strain model for analysis of residual stress and interface stress in laminate composites, J. Compos. Mater. 36 (2002), https://doi.org/10.1177/0021998302036014173.

[30] Z. LI, R.C. BRADT, Thermal expansion and thermal expansion anisotropy of SiC polytypes, J. Am. Ceram. Soc. 70 (1987), https://doi.org/10.1111/j.1151-2916.1987.tb05673.x.

[31] T.R. Pilladi, G. Panneerselvam, S. Anthonysamy, V. Ganesan, Thermal expansion of nanocrystalline boron carbide, Ceram. Int. 38 (2012), https://doi.org/10.1016/j.ceramint.2012.01.016.

[32] Y.S. Touloukian, R.W. Powell, C.Y. Ho, M.c. Nicilaou, Thermophysical properties of matter-the TPRC data series, Thermophys. Electron. Propert. Inf. Anal. Center Lafayette In 11 (1975).

[33] J.D. Eshelby, The determination of the elastic field of an ellipsoidal inclusion, and related problems, Proc. R. Soc. Lond. a Math. Phys. Sci. (1957) 376–396.

[34] T. Mori, K. Tanaka, Average stress in matrix and average elastic energy of materials with misfitting inclusions, Acta Metallurg. (1973) 21, https://doi.org/10.1016/0001-6160(73)90064-3.

[35] G.K. Hu, G.J. Weng, Influence of thermal residual stresses on the composite macroscopic behavior, Mech. Mater. 27 (1998), https://doi.org/10.1016/S0167-6636(97)00050-1.

[36] ASTM Standard C1326-13, Standard Test Method For Knoop Indentation Hardness of Advanced Ceramics, ASTM International, West Conshohocken, PA, 2018, https://doi.org/10.1520/C1326-13R18. www.astm.org, 2013.

[37] ASTM Standard C1161-18, Standard Test Method For Flexural Strength of Advanced Ceramics At Ambient Temperature, ASTM International, West Conshohocken, PA, 2018, https://doi.org/10.1520/C1161-18. www.astm.org.

[38] ASTM Standard C1322-15, Standard Practice for Fractography and Characterization of Fracture Origins in Advanced Ceramics, ASTM International, West Conshohocken, PA, 2019, https://doi.org/10.1520/C1322-15R19. www.astm.org, 2015.

[39] W.W. Chen, B. Song, Split Hopkinson (Kolsky) Bar: Design, Testing and Applications, 2013.

[40] G. Ravichandran, G. Subhash, Critical appraisal of limiting strain rates for compression testing of ceramics in a split Hopkinson pressure bar, J. Am. Ceram. Soc. 77 (1994), https://doi.org/10.1111/j.1151-2916.1994.tb06987.x.

[41] Split-Hopkinson Pressure Bar Testing of Ceramics, in: Mechanical Testing and Evaluation, ASM International, 2018, pp. 497–504, https://doi.org/10.31399/asm.hb.v08.a0003299.

[42] W. Chen, G. Subhash, G. Ravichandran, Evaluation of ceramic specimen geometries used in a split Hopkinson pressure bar, Dyn. Behav. Mater. 1 (1994) 193–210.

[43] C.A. Tracy, Compression test for high strength ceramics, J. Test. Eval. 15 (1987), https://doi.org/10.1520/jte11547j.

[44] F.F. Lange, M. Metcalf, Processing-related fracture origins: II, agglomerate motion and cracklike internal surfaces caused by differential sintering, J. Am. Ceram. Soc. 66 (1983) 398–406, https://doi.org/10.1111/J.1151-2916.1983.TB10069.X.

[45] W. Shoulders, M. Guziewski, J. Swab, To be submitted - effect of microstructure and residual stress on mechanical properties of boron carbide particulate reinforced silicon carbide ceramics, J. Am. Ceram. Soc (n.d.).

[46] B.H. Toby, R.B. Von Dreele, GSAS-II : the genesis of a modern open-source all purpose crystallography software package, J. Appl. Crystallogr. 46 (2013) 544–549, https://doi.org/10.1107/s0021889813003531.

[47] J. ITO, M. IWATSUKI, T. FUKASAWA, Reinvestigation of crystallographic data and X-ray diffraction data of silicon carbide for polytype identification purposes, Bunseki Kagaku (2011), https://doi.org/10.2116/bunsekikagaku.42.8_445.

[48] A.L. Hannam, P.T.B. Shaffer, Revised X-ray diffraction line intensities for silicon carbide polytypes, J. Appl. Crystallogr. 2 (1969) 45–48, https://doi.org/10.1107/s0021889869006510.

[49] O. Sologub, Y. Michiue, T. Mori, Boron carbide, B13-x C2-y (x = 0.12, y = 0.01), Acta Crystallogr. Sect. E Struct. Rep. Online 68 (2012) 1–6, https://doi.org/10.1107/S1600536812033132.

[50] M.W. Chen, J.W. McCauley, J.C. LaSalvia, K.J. Hemker, Microstructural characterization of commercial hot-pressed boron Carbide Ceramics, J. Am. Ceram. Soc. 88 (2005) 1935–1942, https://doi.org/10.1111/J.1551-2916.2005.00346.X.

[51] J.J. Swab, J.J. Pittari, C.S. Meredith, Anisotropy in the compression strength of hot-pressed ceramics, J. Mater. Sci. 58 (2023), https://doi.org/10.1007/s10853-023-09011-3.

[52] E. Medvedovski, Ballistic performance of armour ceramics: influence of design and structure, Part 1, Ceram. Int. 36 (2010) 2103–2115, https://doi.org/10.1016/j.ceramint.2010.05.021.

[53] P. Miranda, A. Pajares, M.A. Meyers, Bioinspired composite segmented armour: numerical simulations, J. Mater. Res. Technol. 8 (2019) 1274–1287, https://doi.org/10.1016/j.jmrt.2018.09.007.

[54] K. Akella, Studies for improved damage tolerance of ceramics against ballistic impact using layers. Procedia Eng, 2017, https://doi.org/10.1016/j.proeng.2016.12.006.

[55] L. Farbaniec, J. Hogan, J. McCauley, K. Ramesh, Anisotropy of mechanical properties in a hot-pressed Boron Carbide, Int. J. Appl. Ceram. Technol. 13 (2016) 1008–1016, https://doi.org/10.1111/ijac.12585.

[56] H. Awaji, T. Watanabe, Y. Nagano, Compressive testing of ceramics, Ceram. Int. 20 (1994) 159–167, https://doi.org/10.1016/0272-8842(94)90034-5.

[57] A. Cosculluela, J. Cagnoux, F. Collombet, Uniaxial compression of alumina : structure, microstructure and strain rate, Le J. de Physique IV 01 (1991) C3109–C3116, https://doi.org/10.1051/jp4:1991314.

[58] A. Cosculluela, J. Cagnoux, F. Collombet, Two types of experiments for studying uniaxial dynamic compression of alumina, Shock Compress. Condens. Matter (1991) 951–954, https://doi.org/10.1016/B978-0-444-89732-9.50220-X, 1992.

[59] A. Rudnick, C.W. Marschall, W.H. Duckworth, B.R. Emrich, The Evaluation And Interpretation Of Mechanical Properties Of Brittle Materials, 1968.

[60] G. Sines, M. Adams, Compression testing of ceramics. Fracture Mechanics of Ceramics, 1978, pp. 403–449.

[61] J. Lankford, The compressive strength of strong ceramics: microplasticity versus microfracture, J. Hard. Mater. 2 (1991) 55–75.

[62] H. Horii, S. Nemat-Nasser, Brittle failure in compression: splitting, faulting and brittle-ductile transition, Philos. Trans. R Soc. Lond. (1986).

[63] J.J. Swab, C.S. Meredith, D.T. Casem, W.R. Gamble, Static and dynamic compression strength of hot-pressed boron carbide using a dumbbell-shaped specimen, J. Mater. Sci. 52 (2017) 10073–10084, https://doi.org/10.1007/s10853-017-1210-7.